Impact of microwave observations on the estimation of Arctic sea surface temperatures

Nielsen-Englyst, Pia; Høyer, Jacob L.; Karagali, Ioanna; Kolbe, Wiebke M.; Tonboe, Rasmus T.; Pedersen, Leif T.

Published in:
Remote Sensing of Environment

Link to article, DOI:
10.1016/j.rse.2023.113949

Publication date:
2024

Document Version
Publisher's PDF, also known as Version of record

Remote Sensing of Environment 301 (2024) 113949

Contents lists available at ScienceDirect

Remote Sensing of Environment

journal homepage: www.elsevier.com/locate/rse

Impact of microwave observations on the estimation of Arctic sea surface temperatures

Pia Nielsen-Englyst [a,b,*], Jacob L. Høyer [b], Ioanna Karagali [b], Wiebke M. Kolbe [a,b], Rasmus T. Tonboe [a], Leif T. Pedersen [a]

[a] DTU-Space, Technical University of Denmark, Lyngby, Denmark
[b] National Centre for Climate Research (NCKF), Danish Meteorological Institute (DMI), Copenhagen, Denmark

ARTICLE INFO

Edited by Menghua Wang

Keywords:
Arctic
Infrared satellite observations
Passive microwave satellite observations
Sea surface temperature (SST)
AMSR-E
AMSR2

ABSTRACT

The frequent and persistent cloud cover in the Arctic limits the extent to which sea surface temperature (SST) can be retrieved from thermal infrared (IR) satellite sensors. Passive microwave (PMW) observations provide highly complementary information to IR, enabling measurements through non-precipitating clouds, although at a coarser spatial resolution. The differences in coverage, accuracy, footprint size, spatial resolution and error characteristics between IR and PMW SSTs require a systematic assessment of how to best combine IR and PMW SST retrievals. This is provided in this study on the basis of the ESA-CCI PMW SST climate data record (CDR) and an existing IR-based gap-free SST and sea ice surface temperature CDR covering the Arctic (>58°N), where cloud cover is a serious limitation to IR sensors. An important step towards a combined IR and PMW SST CDR is to correct for systematic biases in the PMW and IR SST datasets relative to each other. The PMW SSTs show reduced biases against *in situ* SSTs compared to the IR SSTs, but for consistency with time periods when no Arctic PMW SSTs were available, the PMW SSTs have been adjusted to the IR SSTs in this study. This is done using a dynamic bias correction to generate a consistent combined IR and PMW Arctic SST CDR for the period 2002–2017. Including PMW SSTs reduces the standard deviations from 0.54 °C, 0.55 °C and 0.47 °C to 0.47 °C, 0.54 °C and 0.41 °C against drifters, moorings and Argo floats, respectively. The improved performance is seen in almost all regions (including those already covered by IR observations), with the largest improvement in IR data sparse regions. The average theoretical uncertainty reduces by 0.08 °C, which is in good agreement with the observed improvement in the standard deviation against drifters. The results are very promising and expected to improve even further in the future with the launch of the Copernicus Imaging Microwave Radiometer (CIMR), which will enable PMW SST retrievals with lower uncertainties and much closer to coasts and sea ice (where the largest uncertainties arise) than what is possible with previous and current PMW radiometers.

1. Introduction

The sea surface temperature (SST) is an Essential Climate Variable (ECV) used for monitoring, understanding and predicting climate change (Bojinski et al., 2014). The Arctic is warming more rapidly than the global average, due to a number of amplifying feedback mechanisms (e.g. AMAP, 2021; Pithan and Mauritsen, 2014; Meredith et al., 2019; Rantanen et al., 2022), which makes it a very important region to monitor. The extreme environment and the poor accessibility make *in situ* observations challenging and sparse in the Arctic (Centurioni et al., 2019; Donlon et al., 2012).

Satellite observations are an important tool for monitoring the Arctic due to the high spatial and temporal coverage. There are several global satellite-based gap-free (i.e. Level 4, L4) SST products (e.g. Reynolds et al., 2007; Merchant et al., 2019; Donlon et al., 2012), but these usually show large uncertainties and diversity in the Arctic (Dash et al., 2012; Castro et al., 2016; Vazquez-Cuervo et al., 2022), where extreme environmental conditions, limited *in situ* data, persistent cloud cover and a varying length of the sunlit part of the day round the year complicate accurate SST retrievals from satellites (Donlon et al., 2009; Høyer et al., 2012; Minnett et al., 2019). Improving the Arctic SST data has been identified as being of "high priority" for future SST research and developments (O'Carroll et al., 2019). Specialized high latitude algorithms have previously been developed and shown to surpass the global L4 SST products in the Arctic (Jia and Minnett, 2020; Vincent et al., 2008b,a). Moreover, infrared (IR) satellite observations have recently been used to produce the first satellite-based L4 climate data

* Corresponding author at: DTU-Space, Technical University of Denmark, Lyngby, Denmark.
E-mail address: pne@dmi.dk (P. Nielsen-Englyst).

https://doi.org/10.1016/j.rse.2023.113949
Received 24 June 2023; Received in revised form 27 November 2023; Accepted 4 December 2023
Available online 12 December 2023

record (CDR) of combined ocean and sea ice surface temperature in the Arctic (>58°N), which enables consistent climate monitoring of the Arctic warming (Nielsen-Englyst et al., 2023).

The IR SST observations are hampered by clouds, and data gaps usually remain after combining different IR SST datasets. Two common methods used to fill in the data gaps are temporal extension (e.g. Reynolds and Smith, 1994) and spatial interpolation techniques (e.g. Reynolds and Smith, 1994; Thiébaux et al., 2003; Donlon et al., 2012; Nielsen-Englyst et al., 2023). In the Arctic, frequent and persistent cloud cover results in long periods without surface coverage from IR sensors, and the cloud-contaminated observations are often difficult to identify. Therefore, the IR SST analyses usually rely heavily on the choice of interpolation technique and cloud masking in the Arctic, resulting in large sampling errors (Liu and Minnett, 2016). SSTs derived from passive microwave (PMW) observations have the potential to fill in large and persistent data gaps in the IR coverage, since PMW observations are less impacted by clouds and aerosols (Donlon et al., 2007, 2009; Ulaby et al., 2014; Wentz and Meissner, 2000) than IR sensors which nevertheless tend to provide higher spatial resolution. SSTs retrieved from IR sensors usually have spatial resolutions of about 1–4 km and uncertainties of 0.2–0.4 °C (Donlon et al., 2007; Merchant et al., 2019; Reynolds et al., 2002; Embury et al., 2012), while PMW SSTs have spatial resolutions of about 50 km and uncertainties of 0.4–0.5 °C, with the largest uncertainties in high latitudes (Nielsen-Englyst et al., 2018; Alerskans et al., 2020, 2022; Gentemann, 2014; Wentz et al., 2000; Shibata, 2006).

Current and previous PMW sensors do not capture sub-mesoscale to mesoscale SST features and are influenced by land near (~100 km) coasts and sea ice due to the large field of view. Improved spatial resolution of the 6.9 and 10.7 GHz channels could lead to substantial improvements of PMW SST retrievals and their information content in global and regional SST products (O'Carroll et al., 2019). This is one of the primary objectives of the Copernicus Imaging Microwave Radiometer (CIMR) by the European Space Agency (ESA) as a part of the Copernicus Expansion program of the European Union (http://www.cimr.eu/). CIMR will provide high-accuracy, high resolution PMW observations of the Polar Regions, which will enable retrievals of SST at a higher spatial resolution (~15 km) and lower uncertainty (~ 0.3°C) than what is possible with the current PMW missions (Donlon, 2020). In addition to CIMR, the Advanced Microwave Scanning Radiometer 2 (AMSR2) follow-on mission (AMSR3) is currently being prepared by Japan Aerospace Exploration Agency (JAXA) (Kasahara et al., 2020).

The large potential of including high latitude PMW SST retrievals with frequent updates from previous, current and future PMW missions, makes it important to investigate how to best combine IR and PMW SST retrievals in an Arctic analysis. Many global L4 SST analyses already include PMW SST observations e.g. the NOAA Optimum Interpolation (OI) SST V2 (Reynolds et al., 2007; Huang et al., 2021), Operational Sea Surface Temperature and Sea Ice Analysis (OSTIA; Donlon et al., 2012; Good et al., 2020), Canadian Meteorological Center (CMC) SST analysis (Brasnett, 2008), Remote Sensing Systems (REMSS) MW-IR SST product (http://www.remss.com/measurements/sea-surface-temperature/oisst-description), and the Multi-scale Ultra-high Resolution (MUR) SST analysis (Chin et al., 2017). Prior systematic efforts have investigated the impact of including satellite SST retrievals from the IR Advanced Very High Resolution Radiometer (AVHRR), the Advanced Microwave Scanning Radiometer – Earth Observing System (AMSR-E) and the Tropical Rainfall Measuring Mission (TRMM) Microwave Imager (TMI) to an existing *in situ* data based global analysis (Reynolds et al., 2004, 2007), and later the impact of further adding the IR Advanced Along Track Scanning Radiometer (AATSR) and PMW TMI satellite SST retrievals (Reynolds et al., 2010). The AMSR-E data was found to have a strong impact in the mid-latitudes particularly in large gradient regions e.g. the Gulf Stream, because of the improved data coverage (Reynolds et al., 2007). This impact was not seen by adding TMI SSTs, because accurate TMI SST retrievals are limited to the tropics (Reynolds et al., 2010). Similarly, Brasnett and Colan (2016) showed clear improvements when assimilating AMSR2 SSTs in the CMC SST analysis. Other studies have put efforts into characterizing the errors of IR and PMW satellite SST products (O'Carroll et al., 2008; Gentemann, 2014; Ricciardulli and Wentz, 2004) and developing bias corrections to facilitate improved merging of the products using moored and drifting buoys as Castro et al. (2008).

This study presents the first systematic assessment of the impact of including PMW SST observations in an Arctic SST analysis. The PMW SSTs are from the ESA Climate Change Initiative (ESA-CCI) PMW SST CDR (Alerskans et al., 2020) based on AMSR-E and AMSR2 observations. As reference, we use the recently generated Arctic (>58°N) L4 combined SST and sea ice surface temperature (IST) CDR, which uses IR-sensors only (Nielsen-Englyst et al., 2023). Several methods of including satellite PMW SSTs have been tested using one year of data, 2015, in order to identity the best way to combine the SST observations from IR and PMW sensors in the Arctic, aiming for a combined long-term (1982-present) CDR. The year, 2015, was chosen due to a relatively limited IR SST coverage in that year (Merchant et al., 2019). In this case, we would expect the largest impact of including the PMW SST observations and thus, providing the best baseline for testing the different methods. Based on the test runs of 2015, one method has been selected and used for including the PMW SST data in the Arctic reanalysis for the entire ESA CCI PMW SST period (2002–2017). The paper is organized as follows. Section 2 briefly describes the IR-based L4 Arctic SST/IST CDR, the PMW SSTs, and the *in situ* observations used for validation. Section 3 provides a description of the different methods tested for including the PMW SSTs in the Arctic L4 SST/IST dataset. Section 4 presents the impact on satellite coverage, validation results and the effective spatial resolution of the different test runs during 2015. Section 5 provides the validation results and uncertainty estimates based on the combined IR and PMW Arctic L4 SST CDR (2002–2017). Section 6 discusses the results and provides suggestions for future work and finally, the conclusions are provided in Section 7.

2. Data

2.1. L4 Arctic SST/IST

This study uses the combined L4 Arctic (>58°N) SST/IST climate dataset (described in Nielsen-Englyst et al., 2023) as baseline. The dataset covers both sea and sea-ice surfaces in the Arctic, with open ocean being defined by sea ice concentration (SIC) ≤ 15%, the marginal ice zone (MIZ) as 15% < SIC ≤ 70%, and ice covered when SIC> 70%. The long term (1982–2021) climate dataset was generated by combining multiple sources of satellite observations and applying a statistical optimal interpolation (OI) method to obtain daily gap-free fields, with a spatial resolution of 0.05° in latitude and longitude. The input SST data consist of SST observations from A(A)TSR, AVHRR and SLSTR (Sea and Land Surface Temperature Radiometer) from Copernicus Climate Change Service (C3S) and ESA-CCI projects (Merchant et al., 2019), while the IST observations are obtained from the Arctic and Antarctic ice Surface Temperatures from thermal Infrared satellite climate dataset version 2 (AASTI v2; Dybkjær et al., 2014) and from the operational Ocean and Sea Ice Satellite Application Facility (OSI SAF) IST product (OSI-205; Dybkjær et al., 2018). To be included in the OI processing, a minimum quality level (QL) of 4 was required for all observations except from those from SLSTR, where a QL of 5 was required (Nielsen-Englyst et al., 2023). The observations were combined and averaged (i.e. using a noise weighting average) by considering the available data within 24 h from the analysis. The gaps in the resulting fields were filled by the OI method using the previous day's analysis field as first guess. For each grid cell, the OI method is designed to provide the optimal SST/IST value, given statistical

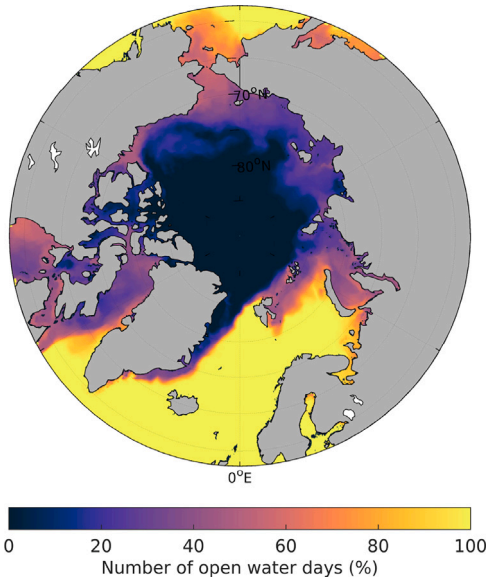

Fig. 1. Example of the number of open water days (%) during one year (2015).

input, such as first guess variance, error covariances, uncertainties on the input observations and correlation functions, which were derived empirically from the observations (Nielsen-Englyst et al., 2023). Spatially varying correlation functions in the latitudinal and longitudinal directions were derived and used in the OI processing, with e-folding scales of 69.5 km, 276.1 km and 344.4 km for SST, IST, and the MIZ, respectively (Nielsen-Englyst et al., 2023). A multi-SIC field was used to identify the different surface types for each day during the record. A temporally and spatially constant bias correction (of +0.16 °C) was applied in the post-processing of the L4 SST fields to correct for the mean difference in the derived L4 SSTs, when compared to drifting buoys SSTs for the period 1982–2021. This difference arises since the IR SSTs are too cold, and this will be further discussed in Section 6. Each daily L4 Arctic SST/IST field comes with a theoretical uncertainty estimate, which has been derived directly from the OI method (Nielsen-Englyst et al., 2023). Validation of the OI-derived L4 SST uncertainties against drifting buoy observations showed that the OI method is capable of deriving reliable uncertainty estimates for SST (Nielsen-Englyst et al., 2023). The L4 Arctic SST/IST processing system will be referred to as the DMI OI L4 processing system and more details on its configuration is available in Nielsen-Englyst et al. (2023).

Fig. 1 shows an example of the number of open water days during one year (2015), while Fig. 2 shows the corresponding seasonal variation in the open water fraction (dark blue + light blue). During winter and spring, only 20% of the (non-land) surface is open water, while the open water coverage increases to almost 60% during September. Fig. 2 also illustrates the percentages of the open ocean and sea ice (including the MIZ) grid cells which are satellite-observed and unobserved for each day during 2015. About 75% of the sea ice covered grid cells are covered with observations during winter, while the IST satellite coverage drops to below 10% during summer due to an extensive summer cloud cover. On average, only 21.7% of the open ocean is covered with satellite observations. During winter, only ~10% of the open ocean grid cells are covered by observations, while the open ocean satellite coverage reaches a maximum in summer of about 35%. This means that the L4 SST/IST CDR is actually based on a very limited set of satellite observations during long periods of the year. In this study, the focus is on the open ocean regions because of the variable sea ice emissivity, and the fact that thermal microwaves penetrate into the snow-cover on sea ice (Ulaby et al., 1986; Tonboe et al., 2011). The penetration in sea ice means that the IST measured by IR and PMW radiometers is not the same (Lavergne et al., 2022), which complicates a blend of the two (see Section 6).

In 2015, the L4 SST CDR is based only on IR satellite observations from AVHRR sensors (Nielsen-Englyst et al., 2023). Fig. 3(a) shows the total number of days with IR SST observations in each grid cell during 2015, and it is evident that IR observations of the surface are limited by clouds in many regions for more than half of the year.

2.2. PMW data

We use the Level-2 (L2) data from the PMW SST CDR described in Alerskans et al. (2020) and developed within the ESA-CCI SST project (Merchant et al., 2014). The L2 PMW SST CDR is generated using a statistical regression-based retrieval algorithm, which uses observations from AMSR-E and AMSR2 for the period June 2002–October 2017 (Alerskans et al., 2020). The PMW SSTs have been adjusted to best represent the daily mean temperature at 20 cm depth for consistency with the ESA-CCI IR SST retrievals (Embury et al., 2012; Merchant et al., 2019). The resulting L2 PMW SST CDR is provided with a 10 km grid resolution and is available from the Centre for Environmental Data Archival (CEDA) at http://gws-access.ceda.ac.uk/public/esacci-sst/PMW2.0_release/AMSR/L2P/.

In this study, only PMW SST observations assigned QL 3–5 are used. For these QLs, no PMW SSTs are retrieved if any sea ice is detected within ±200 km (using the ERA-Interim SIC), or if land is detected within ±100 km (Alerskans et al., 2020). This is done to exclude PMW SST retrievals which may be contaminated by land and sea ice due to the large satellite footprint at low frequencies. Fig. 3(b) shows the total number of days with PMW observations during one year (2015), when included in the OI processing scheme in a similar way as the IR observations. The large band with no PMW observations along the coasts and the sea ice edge is explained by the fact that only the highest (3-5) QLs are used. In larger distances from coasts and sea ice, the PMW SST observations show superior coverage compared to the IR SST retrievals, which are limited by cloud cover. This illustrates the large potential there may be in combining IR and PMW observations for the SST mapping of the Arctic.

2.3. *In situ* observations

In situ observations from drifting buoys, moored buoys and Argo floats are used for validation as in Nielsen-Englyst et al. (2023). The *in situ* observations are obtained from the Hadley Centre Integrated Ocean Database v. 1.2.0.0 (HADIOD, Atkinson et al., 2014). The drifters are well represented in the Arctic open ocean region. The Argo floats show good coverage in the North Atlantic and Greenland Sea while the moorings which are concentrated in certain regions of the North Atlantic and southern Greenland Sea. In this study, the *in situ* observations are only used for validation and have not been included in the analysis nor used for bias correction of the analysis as was done using the drifters in Nielsen-Englyst et al. (2023).

3. Methods

Satellite IR and PMW radiometers measure top-of-the-atmosphere up-welling thermal emission. However, the IR and PMW satellite SST observations have very different characteristics in terms of spatial resolution and sensitivity to noise sources, which need to be taken into account in order to combine the two data sets properly (Castro et al., 2016). One difference is, as already mentioned, the almost all-weather capability of PMW observations compared to the clear-sky only capability of IR observations. The penetration depth of IR and PMW sensors also differs, with IR measuring the skin SST and PMW sensors measuring the subskin temperature (Donlon et al., 2007; Minnett and Kaiser-Weiss, 2012). However, the L2 IR and PMW SST datasets used in this study have already been adjusted to best represent the daily mean

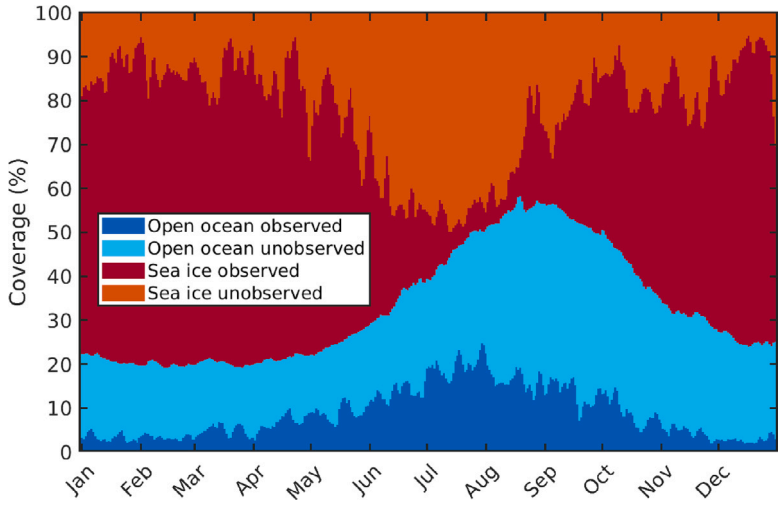

Fig. 2. Example of the coverage (%) of the open ocean and sea ice (including the MIZ) grid cells, which are satellite-observed and unobserved, respectively, for each day during one year (2015).

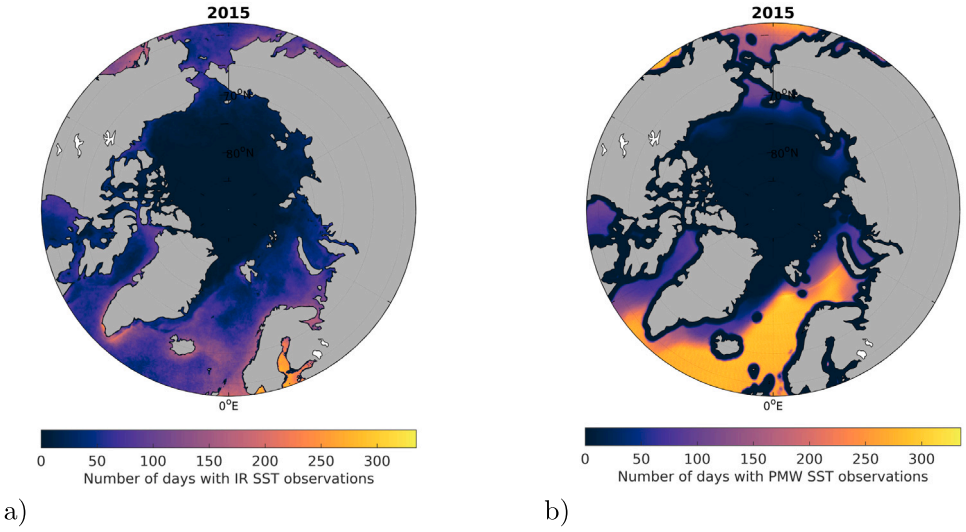

Fig. 3. The total number of days with SST observations during 2015 from (a) IR and (b) PMW sensors.

at the same depth (of 20 cm) by the data providers, using physical modelling of the diurnal cycle (Embury et al., 2012; Horrocks et al., 2003; Merchant et al., 2019). The IR and PMW observations are also subject to different sources of uncertainty. The Arctic IR SST uncertainties arise mainly due to undetected clouds and insufficient representation of the atmospheric attenuation (e.g. by water vapour) (Castro et al., 2008), while large PMW SST uncertainties usually are related to rain, strong winds (>20 m s^{-1}), sun-glint, radio frequency interference (RFI), sidelobe contamination near (typically within ~100 km) land and/or sea ice (Gentemann, 2014; Gentemann and Hilburn, 2015). Other differences are related to the different grid and spatial resolutions. The IR SST datasets used in this case have grid resolutions of 0.05° (corresponding to 5 km in the latitudinal direction and to ~3.9 km and ~1.9 km in the longitudinal direction at 58°N and 80°N, respectively), which is close to the actual spatial resolution of the observations. On the other hand, the ESA-CCI L2 PMW SST data is provided with a 10 km grid resolution, while the actual spatial resolution is in the order of 50 km due to the large satellite footprint at low frequencies. Because of the large PMW footprint, PMW SSTs are not retrieved close to coasts and sea ice (for QL 3–5), and in these areas, the IR observations are thus the only source of SST observations (Alerskans et al., 2020). The different PMW and IR footprint sizes make it important to assess the impact on the effective spatial resolution when blending PMW and IR SSTs.

In this study, different test runs have been designed to assess the best method to include the PMW SST observations in the Arctic L4 SST/IST reanalysis taking into account the differences in the observation characteristics between the IR and PMW observations. All test runs were processed using the DMI OI L4 processing system (Section 2.1), which is described in detail in Nielsen-Englyst et al. (2023). The DMI OI L4 processing system takes the L2 satellite observations as input and averages these into single sensor daily Level-3 (L3) fields. The L3 fields are afterwards aggregated into L3 super-collocated (L3S) fields by calculating the noise weighted average of the available observations within 24 h from the analysis. The IR SSTs are assumed to have uncertainties of 0.3 °C (ATSR), 0.4 °C (AVHRR), 0.4 °C (SLSTR) (following Nielsen-Englyst et al., 2023), while the PMW SSTs are assumed to have uncertainties of 0.5 °C (Alerskans et al., 2020). The L4 fields are generated using the same empirically derived OI statistical parameters as in Nielsen-Englyst et al. (2023) for all test runs. The temporally and spatially constant bias correction (of +0.16 °C) as applied in Nielsen-Englyst et al. (2023) has been excluded in the test runs to present the non-(in situ)adjusted validation results for a fair comparison of the IR and PMW derived SST datasets. Table 1 provides an overview of the

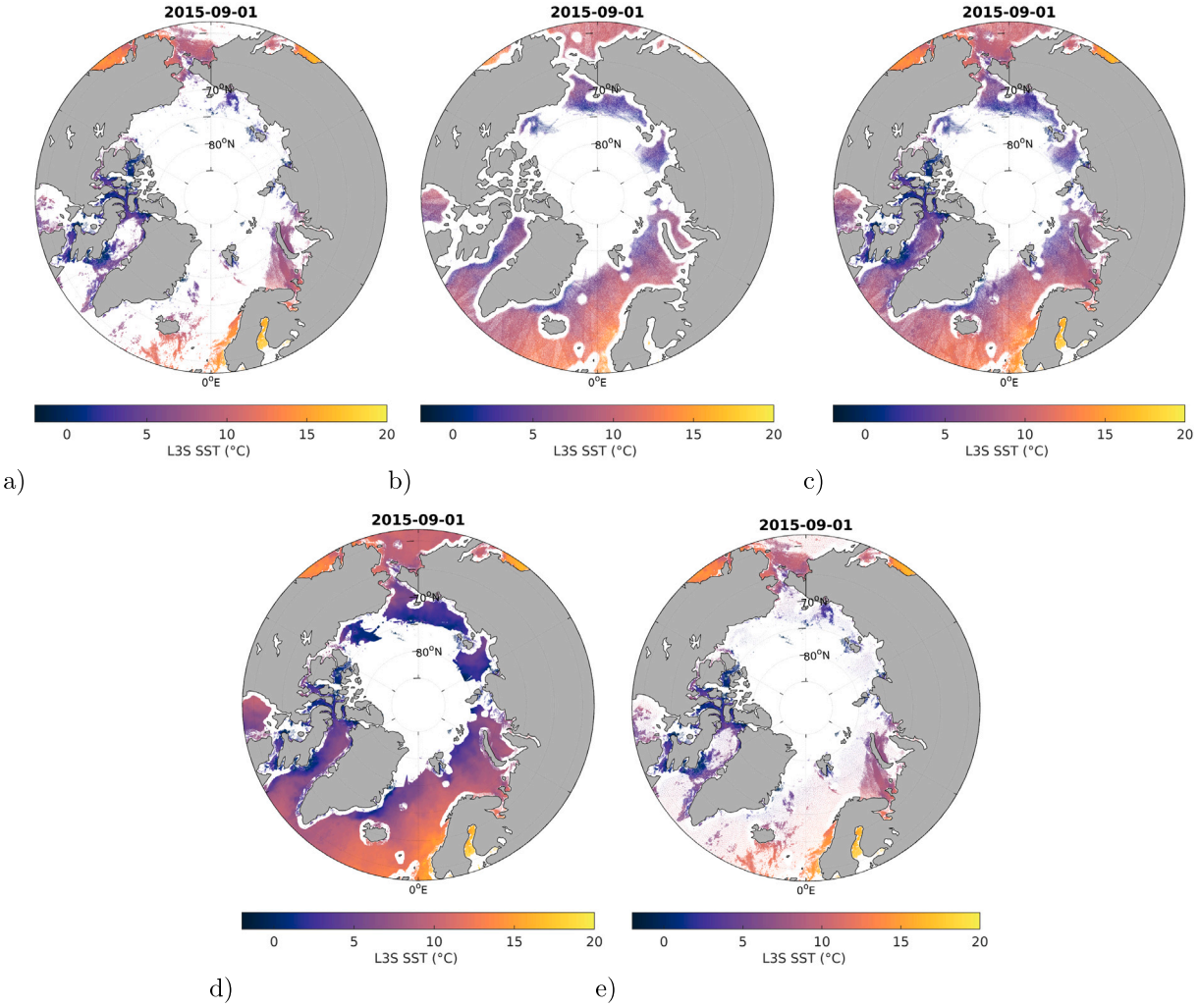

Fig. 4. Examples illustrating the L3S SST field during one day i.e. September 1, 2015 for the testruns (a) IR, (b) PMW, (c) IR_PMW, (d) IR_PMW_AVG and (e) IR_PMW_SUB.

different test runs processed for 2015, while a description of each test run is provided below.

3.1. IR only (IR)

Test run IR is identical to the Arctic SST/IST CDR described in Nielsen-Englyst et al. (2023) except that the constant bias correction (of +0.16 °C) against drifters has been excluded (as stated in the previous section). This IR-only test run is used as reference for the following test runs, which all include PMW observations. Fig. 4(a) shows an example of the L3S SST field during one day (September 1, 2015) when only IR SST observations are used in the aggregation, leaving large regions unobserved due to clouds.

3.2. PMW only (PMW)

Test run PMW excludes all IR SST data and is based only on the PMW SST data. In this case, the PMW observations have been included using the same approach as was done for the IR observations in the first test run. When aggregating to single sensor L3 fields, this leaves gaps in approximately every second grid cell of the L3 PMW field, since the L2 PMW observations are provided at a 10 km grid (in contrast to the L4/L3 0.05 degree grid), and a given satellite observation is only included once in the current DMI OI L4 processing scheme. Fig. 4(b) shows an example of the resulting L3S SST field, illustrating superior coverage compared to test run IR in all regions, except from near coasts and sea ice.

Table 1
Overview of the different test runs. The IR headline refers to IR being included as in Nielsen-Englyst et al. (2023), while the PMW headline refers to PMW being included in a similar way as IR. PMW-AVG specifies that a complete and averaged PMW field is included. In contrast, PMW-SUB corresponds to a sub-sampled PMW field being included. REF indicates if an inter-sensor bias correction has been used and specifies the applied reference sensor. See Sections 3.1–3.7 for a detailed description of each test run.

Test run	IR	PMW	PMW-AVG	PMW-SUB	REF
IR	X				
PMW		X			
IR_PMW	X	X			
IR_PMW_AVG	X		X		
IR_PMW_SUB	X			X	
IR*_PMW	X		X	X	IR
IR_PMW*	X		X	X	PMW

3.3. IR and PMW (IR_PMW)

Test run IR_PMW is the first attempt to combine IR and PMW SST observations in the DMI OI L4 processing scheme. The IR and PMW observations have been included as in the first two test runs, leaving gaps in approximately every second grid cell of the L3 PMW field. Fig. 4(c) shows the resulting L3S SST field, illustrating the superior coverage obtained by combining the IR and PMW SST observations. IR_PMW will be the baseline of the following test runs, which all combine the IR and PMW observations using slightly different approaches.

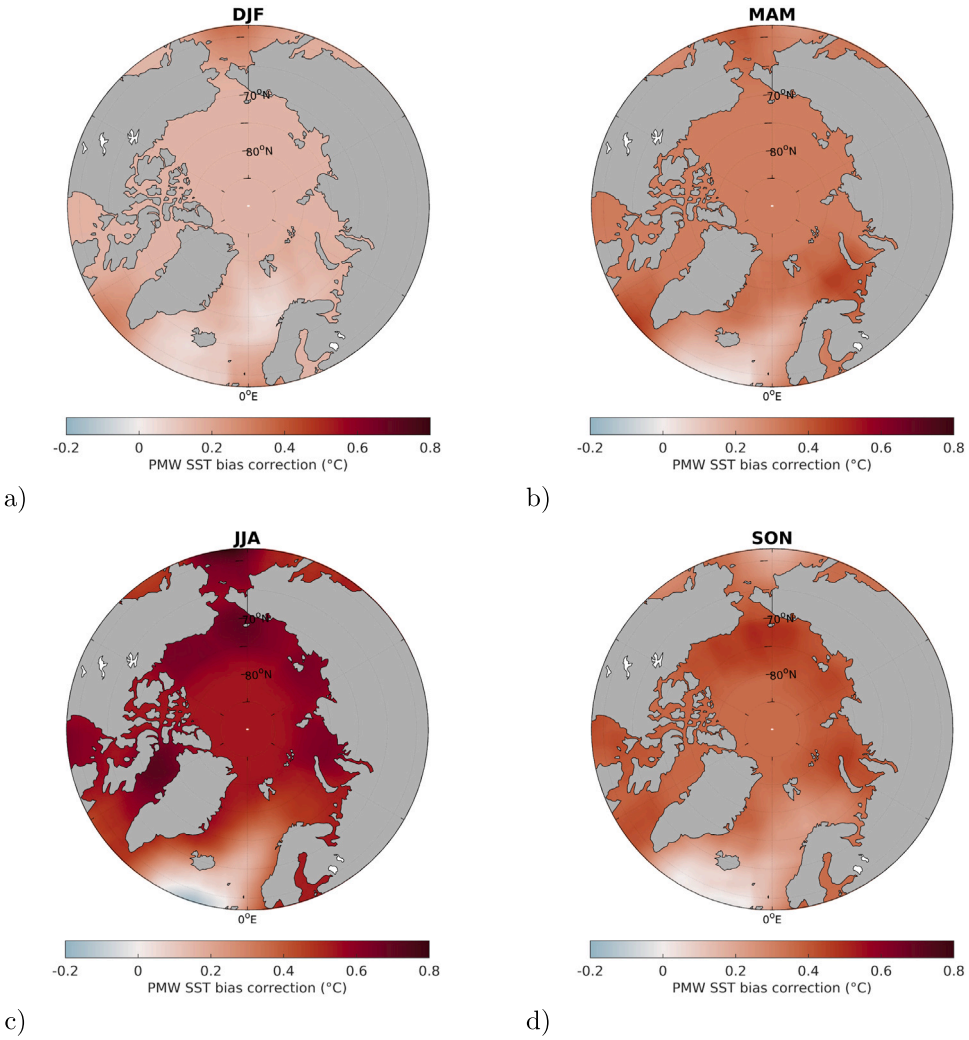

Fig. 5. Spatial variation of the mean coarse grid (and extrapolated) PMW SST bias correction field for the months (a) December–February (DJF), (b) March–May (MAM), (c) June–August (JJA), and (d) September–November (SON), 2015. The PMW SST bias correction field is subtracted from the PMW SST observations in IR*_PMW (and added to the IR SST observations in IR_PMW*).

3.4. IR and averaged PMW (IR_PMW_AVG)

IR_PMW_AVG is tested to see the effect of a more complete PMW SST field. The setup is similar to IR_PMW, but differs in the way the L3 PMW field is aggregated. Instead of only allowing each satellite observation to be included once, each L2 PMW satellite observation is included in all L3 grid cells within a radius of 5 km. Since the grid resolution of 0.05° corresponds to less than 4 km in the longitudinal direction in the Arctic (>58°N), this approach allows observations in all grid cells covered by the PMW footprints of the L2 observations and increases the number of L2 PMW observations available in each L3 grid cell in general. Fig. 4(d) shows the averaged and more complete L3S SST field obtained by using this setup.

3.5. IR and subsampled PMW (IR_PMW_SUB)

Two problems arise in the previous test runs including PMW SSTs. Firstly, the L3 PMW SST grid cells are substantially over-sampled (with the L2 grid resolution being much higher than the PMW footprint) and each L3 PMW SST grid cell is thereby not independent but noise-correlated with its neighbouring grid cells (within the satellite footprint of ~50 km). Moreover, there is a risk of PMW flooding in the OI scheme, and thus, minimizing the impact of the much less frequent IR SSTs. Test run IR_PMW_SUB investigates the effect of sub-sampling the L2 PMW SST observations. In IR_PMW_SUB, the L2 PMW SST observations have been sub-sampled with a step of four in the longitude and latitude of the L2 grid before averaging to the L3 PMW fields. This minimizes the dependence between the L3 PMW grid cells, and reduces the amount of L3 PMW grid cells and the risk of L3 PMW SST flooding in the OI scheme. Fig. 4(e) shows an example of the resulting L3S SST field using the IR SST observations and the sub-sampled L2 PMW SST observations as input.

*3.6. IR and averaged, subsampled and IR-adjusted PMW (IR*_PMW)*

The rationale behind IR*_PMW is to use the averaged and complete L3 PMW fields produced during test run IR_PMW_AVG but by applying a mask to these fields (based on the IR_PMW_SUB L3 PMW fields) to minimize the dependence between the PMW observations and the risk of L3 PMW SST flooding in the OI scheme. Therefore, only those L3 PMW grid cells, which are included in IR_PMW_SUB are kept and included in the L3S and L4 generation of test run IR*_PMW. This means that the number of days with observations is the same as in IR_PMW_SUB and the L3S SST coverage is identical to the SST coverage visually implied in Fig. 4(e).

IR*_PMW also includes an inter-sensor bias correction, which has been implemented to correct for systematic biases in the IR and PMW SST data sets relative to each other. This is an important step towards

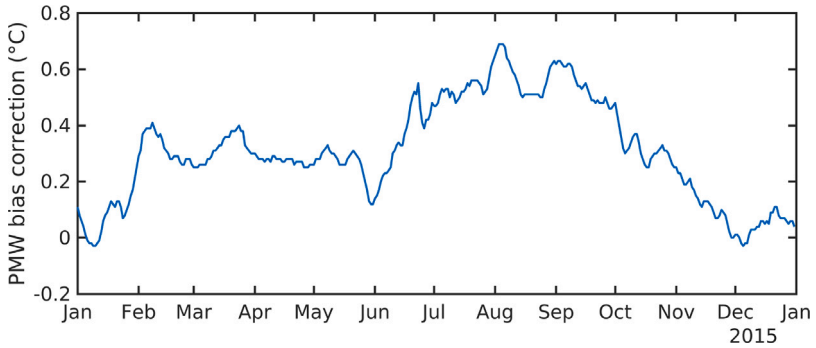

Fig. 6. Seasonal variation of the daily spatially mean (>58°N) PMW bias correction field subtracted from the L3 PMW SST observations in IR*_PMW (and added to the IR SST observations in IR_PMW*) during 2015.

a combined IR and PMW dataset to avoid introducing biases when switching from one sensor to the other/or both. Here, the L3 PMW SST data have been corrected using the L3 IR SST observations as references (the "*" in IR*_PMW denotes the reference field). The bias correction is described in more detail in Section 3.8.

3.7. PMW-adjusted IR and averaged, subsampled PMW (IR_PMW*)

IR_PMW* is similar to IR*_PMW, but instead of correcting the PMW SST observations against IR SST, the IR SST observations have been corrected against the PMW SST observations.

3.8. Inter-sensor bias correction

In test run IR*_PMW and IR_PMW*, an inter-sensor bias correction has been implemented to correct for systematic biases in the IR and PMW SST data sets relative to each other. The inter-sensor bias correction method was developed in Høyer et al. (2014), where it was demonstrated to be very efficient in removing biases throughout the year. The bias correction is assumed to be a smooth field, mainly accounting for slowly varying systematic tendencies of each sensor retrieval.

Using IR as reference, the following approach is used to estimate the PMW SST bias correction (subtracted from the L3 PMW observations in IR*_PMW). The IR SST reference field has been averaged onto coarser grid (0.25°) and aggregated using a temporal window of 7 days. A difference field is calculated for each day by subtracting the IR reference field from the corresponding coarse resolution aggregated PMW sensor field. This coarse resolution difference field is afterwards interpolated to high resolution (0.05°) and smoothed over 500 km. The 500 km smoothing scale has been chosen to reduce small scale noise to ensure a robust bias correction and to capture the expected scale of the biases in the satellite retrievals, which may be due to synoptic atmospheric events. The resulting high resolution difference field has been used to bias-correct the L3 PMW SST fields. The bias correction has been subtracted from the L3 PMW observations in IR*_PMW. In IR_PMW*, the bias correction is calculated in a similar way using PMW as reference field, which corresponds to adding the PMW bias correction to the L3 IR SST observations. Fig. 5 shows the seasonal spatial variation of the coarse grid, smooth and extrapolated PMW SST bias correction field, while Fig. 6 shows the daily mean PMW SST bias correction throughout the year 2015. In all seasons, the bias correction is smallest in the North Atlantic. The average bias correction is 0.31 °C, with almost no correction during winter and a maximum during summer of about 0.6 °C.

4. Test run results

This section investigates the impact on the satellite coverage, validation and the effective spatial resolution by including PMW SST observations in the Arctic L4 SST/IST dataset using one year (2015) of the data and the setup from the test runs described in Section 3.

4.1. Satellite coverage

The number of daily satellite observations included in the OI processing scheme varies among the test runs. Fig. 7 shows the change in the number of daily SST observations compared to the IR reference test run for the individual test runs during 2015. In the case where only PMW observations are used (Fig. 7(a)), no SST observations are available near coasts and sea ice, but more SST observations are available everywhere else compared to test run IR. Combining PMW and IR observations as in IR_PMW (Fig. 7(b)), most regions (away from coasts and sea ice) experience more SST observations compared to test run IR. Performing the L3 PMW averaging by including more L2 PMW observations as in IR_PMW_AVG allows many more days with SST observations compared to the other test runs (Fig. 7(c)). Fig. 7(d) shows the remaining number of days with SST observations after the L3 PMW fields have been sub-sampled to only include the available L3 PMW grid cells from IR_PMW_SUB. The average daily SST coverage for the different test runs are: 21.7% (IR), 33.9% (PMW), 55.6% (IR_PMW), 73.8% (IR_PMW_AVG) and 25.2% (IR_PMW_SUB/IR*_PMW/IR_PMW*) during 2015.

4.2. Validation

The different test runs have been validated against drifting buoy SST observations, which provide the best representation of the Arctic. Table 2 shows the validation results of the L4 SST fields, the aggregated L3 super-collocated (L3S) SST fields, and the single sensor L3 PMW SST fields during 2015. Matchups with drifter SST or L4/L3S/L3 SST below −1.8 °C and matchups with L4/L3S/L3 – drifter SST differences deviating more than three times the standard deviation from the mean L4/L3S/L3 – drifter SST difference (referred to as a 3-sigma filter) have been excluded from the validation statistics. The filters are applied to exclude erroneous *in situ* observations and to provide more representative validation statistics (without dominance from outliers). Each filter removes about 2% of the L4 matchups. The varying satellite coverage (as seen in Section 4.1) is reflected in the large variations in the number of L3S and L3 PMW matchups in Table 2.

For test run IR, a significant increase in standard deviation is seen from the L3S to L4 field, which indicates that it is difficult for the OI processing to provide accurate SSTs in the poorly IR observed regions. The L4 IR mean SST difference of −0.14 °C is close to the difference (of −0.16 °C), which was documented and corrected for in the post-processing of the long-term climate dataset in Nielsen-Englyst et al. (2023). As seen in Fig. 6, the PMW observations are generally warmer than the IR observations, and the resulting mean difference against drifters is reduced for all test runs where PMW observations are included in the L4 generation (and not referenced against the IR observations as in IR*_PMW). All combinations of IR and PMW observations show reduced L4 standard deviations compared to only using either IR or PMW SST observations.

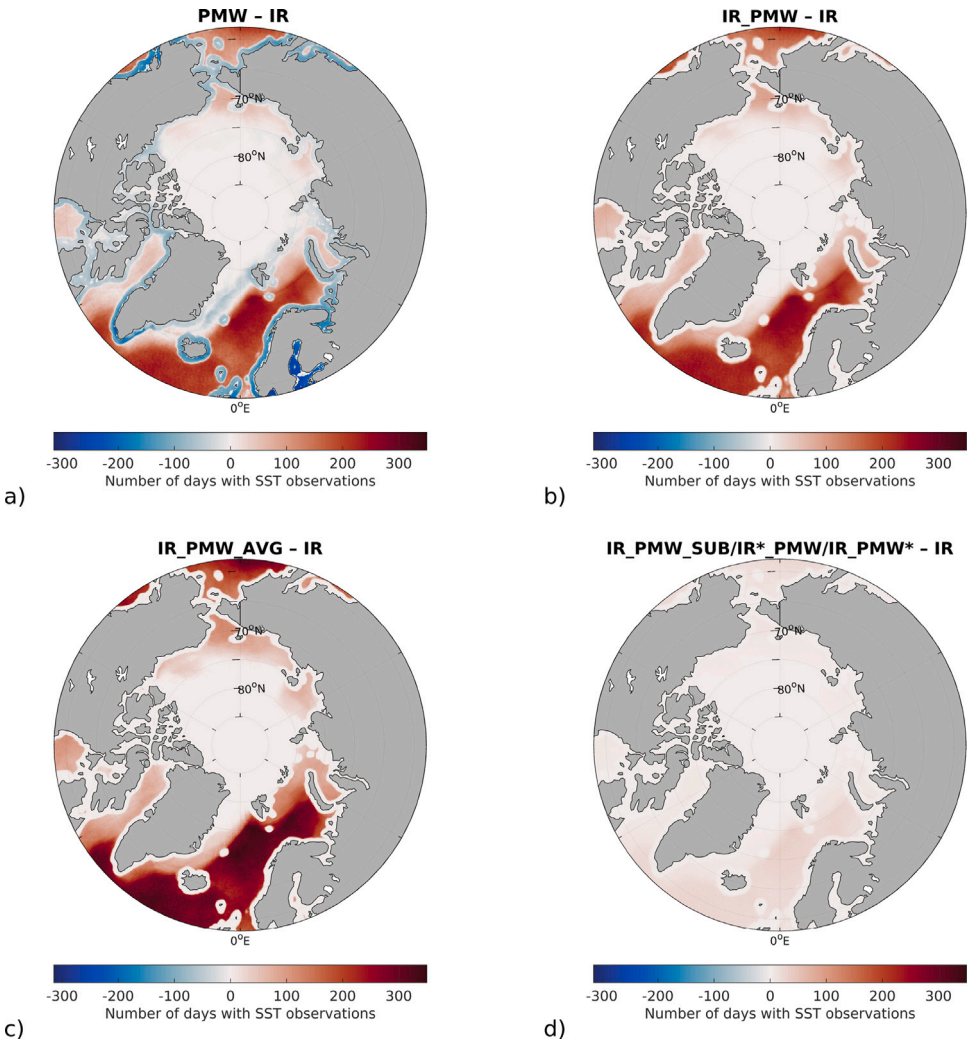

Fig. 7. Differences in the total number of daily SST observations compared to test run IR for (a) PMW, (b) IR_PMW, (c) IR_PMW_AVG and (d) IR_PMW_SUB/IR*_PMW/IR_PMW* during 2015.

Table 2
Overall performance of the different test runs against *in situ* observations from drifting buoys during 2015. The table shows the mean difference (MD; provided as satellite fields minus *in situ*), standard deviation of the differences (STD), root mean squared difference (RMSE), and the number of observations (Nobs) for the L4, the aggregated L3 super-collocated (L3S) and single-sensor L3 PMW SST fields, respectively. A 3-sigma filter has been applied to remove outliers.

Test run	L4				L3S				L3 PMW			
	MD	STD	RMSE	Nobs	MD	STD	RMSE	Nobs	MD	STD	RMSE	Nobs
IR	−0.14	0.64	0.65	193,798	−0.10	0.47	0.48	41,312	–	–	–	–
PMW	−0.03	0.74	0.74	192,140	−0.01	0.57	0.57	97,648	−0.01	0.57	0.57	97,648
IR_PMW	−0.04	0.56	0.57	194,434	−0.03	0.54	0.54	119,014	−0.01	0.57	0.57	97,649
IR_PMW_AVG	−0.03	0.56	0.56	194,457	−0.02	0.47	0.47	153,197	−0.00	0.48	0.48	140,401
IR_PMW_SUB	−0.06	0.56	0.56	194,188	−0.08	0.51	0.51	49,506	0.00	0.63	0.63	10,256
IR*_PMW	−0.18	0.56	0.59	194,159	−0.12	0.47	0.48	49,450	−0.01	0.44	0.44	10,219
IR_PMW*	0.05	0.56	0.56	194,532	0.12	0.48	0.49	49,456	−0.01	0.44	0.44	10,219

Table 2 also shows that it is possible to reduce the standard deviations of the L3 PMW observations by including more (of the surrounding) L2 PMW observations in the aggregation of the L3 PMW field. This also allows more L3 grid cells to be assigned with a PMW SST and results in more L3 PMW matchups compared to PMW/IR_PMW. The opposite is the case when the L2 PMW fields are sub-sampled. Here the number of grid cells with a L3 PMW SST is reduced, which results in fewer matchups than for PMW/IR_PMW, and less L2 PMW observations available for averaging the L3 PMW SST fields, resulting in a larger L3 PMW SST standard deviation. If the L3 PMW SST validation subset from IR_PMW_SUB (10,256 matchups) is used for the IR_PMW_AVG L3 PMW SST validation, the standard deviation and bias reduce to 0.44 °C and −0.01 °C (as also seen for IR*_PMW/IR_PMW*). This clearly shows that including more L2 PMW SST observations in the L3 PMW SST aggregation improves the L3 PMW SST performance substantially.

The improved L3 PMW and L3S standard deviations of IR*_PMW/IR_PMW* (and IR_PMW_AVG) are, however, not reflected in the L4 standard deviations, which do not vary among the test runs including both PMW and IR SST observations. If only the L3S matchups of IR_PMW_AVG (153,197 matchups) are considered in the L4 validation, all combined IR and PMW test runs provide equal same standard deviations of 0.46 °C, while test run IR and test run PMW provide standard deviations of 0.53 °C and 0.55 °C, respectively (not shown). This indicates that if both IR and PMW observations are

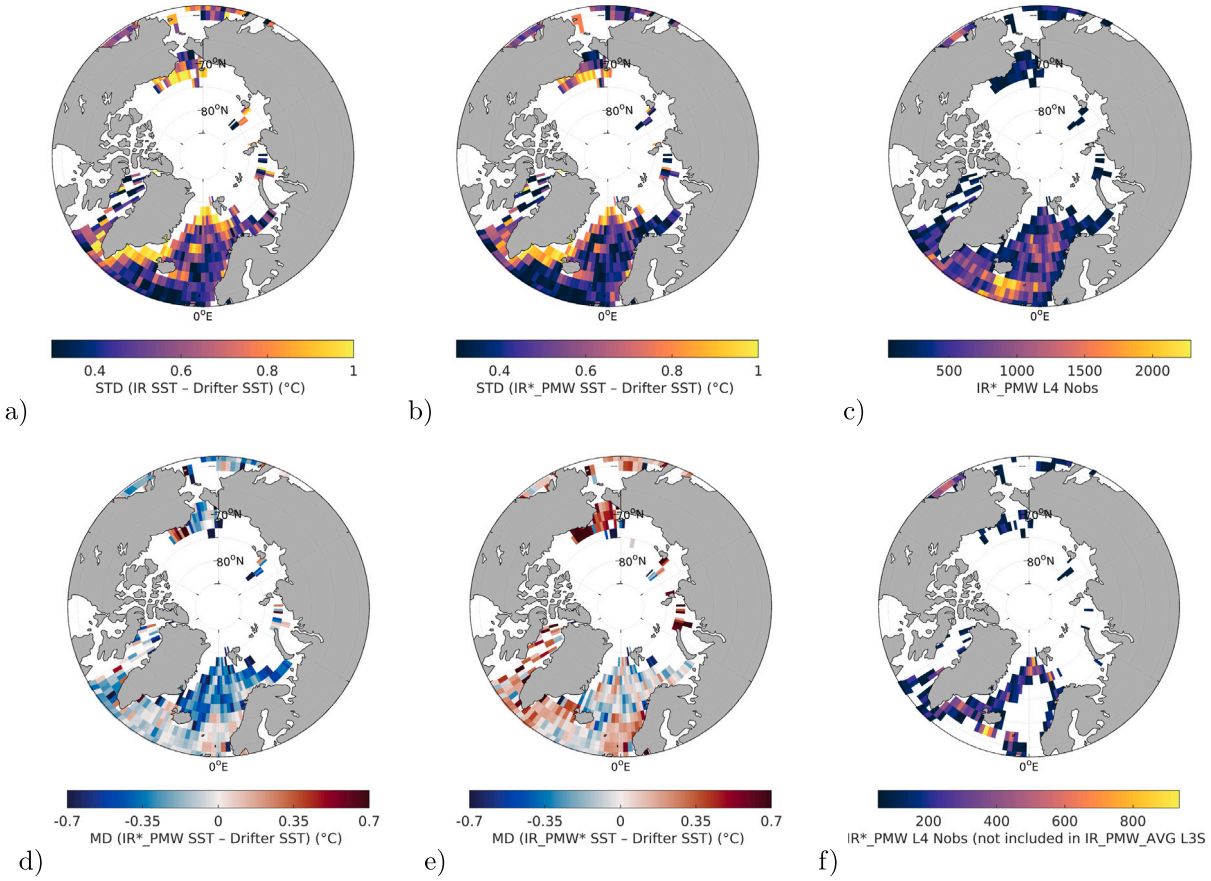

Fig. 8. The standard deviation (STD) of the L4 SST differences against drifter SST for (a) IR and (b) IR*_PMW, and the mean differences (MD) between (d) IR*_PMW, (e) IR_PMW* and drifters. The last column shows the number of L4 matchups (Nobs) for (c) IR*_PMW and (f) IR*_PMW which are not included in the IR_PMW_AVG L3S matchups. The statistics are calculated for each 2 × 2 degree grid having more than 50 members during 2015.

included, the OI L4 processing is able to provide accurate SSTs for those 153,197 matchups despite the differences in the L3S and L3 PMW fields.

Figs. 8(a) and 8(b) show the geographical distribution of the standard deviations of the L4 SST differences against drifting buoy SST using IR and IR*_PMW SST, respectively, with the latter being similar to IR_PMW, IR_PMW_AVG, IR_PMW_SUB, and IR_PMW* (which are not shown). In both cases, the largest standard deviations are found along the coasts and in the seasonal ice covered waters. The few or none satellite observations from the IR and PMW sensors in these regions (see Fig. 3) make it difficult for the OI method to provide accurate SSTs. Figs. 8(d) and 8(e) show the mean differences in 2015, when compared to drifting buoy SST for IR*_PMW and IR_PMW*, which have been selected to illustrate the impact on the MD when the satellite observations are corrected against IR and PMW observations, respectively. Large differences are seen in the mean SST differences for IR*_PMW and IR_PMW*, with IR*_PMW being cold compared to drifters, with an increasing magnitude towards the sea ice edge. In contrast, IR_PMW* shows varying mean differences, with an average difference around zero, but also regions with SSTs warmer than drifters (e.g. the Beaufort and Chukchi Sea). Fig. 8(c) shows the distribution of the L4 matchups (with drifters) available for validation of IR*_PMW during 2015, which is similar to the matchup distribution of the other test runs (not shown). The drifter matchups show good coverage of the open water regions with most matchups in the North Atlantic and southern Greenland Sea. Fig. 8(f) shows the distribution of those IR*_PMW L4 matchups that are not part of the IR_PMW_AVG L3S matchups i.e. those matchups that have no IR or PMW satellite SST observations within the corresponding grid cells. These are concentrated along the coasts and sea ice edge. In these regions, increased standard deviations are observed for both IR and IR*_PMW (Figs. 8(a) and 8(b)) as well as for the other test runs (not shown). This will be discussed in greater detail in Section 6.

The performances of IR, IR*_PMW and IR_PMW* are shown as a function of latitude (Fig. 9(a)) and time (Fig. 9(b)) for 2015. The shaded areas represent the 95% confidence intervals (Thomson and Emery, 2014) and it is evident that the differences among the test runs are significant, even at high latitudes where the least matchups are available. Generally, IR*_PMW/IR_PMW* show smaller standard deviations, with the largest improvement between 68°N and 80°N compared to test run IR. Test run IR and IR*_PMW show a gradual increase in the absolute mean difference with latitude. This is in contrast to IR_PMW*, which shows a mean difference centred around zero except from northwards of about 80°N, where it is colder than drifters, but to a smaller degree than the IR and IR*_PMW. IR_PMW* also shows a smaller and more stable mean difference as a function of time compared to test run IR and IR*_PMW (Fig. 9(b)). The dynamic bias correction of IR against PMW is thus able to significantly reduce the latitudinal and seasonally discrepancy observed in the IR SSTs.

4.3. Spectral analysis

Due to the differences in IR and PMW footprint sizes and coverage, it is important to assess the impact on the effective spatial resolution of the L4 product, when ingesting the PMW SSTs into the IR-based L4 SST/IST analysis. Therefore, a spectral analysis has been performed in the two sub-domains shown in Fig. 10 for the different L4 SST test runs. Comparisons of the spectral power will indicate added benefit in resolving SST signals or degradation of the effective spatial resolution when including the coarser PMW observations. In addition, they may

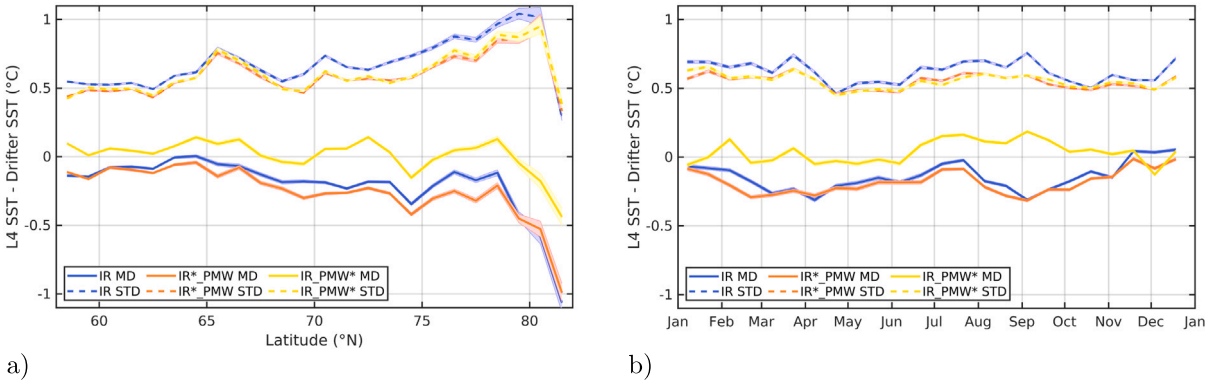

Fig. 9. Mean differences (MD) and standard deviations (STD) of the differences using drifter SST as reference during 2015 for test run IR, IR*_PMW and IR_PMW* as a function of (a) latitude (°N) and (b) time, using bin sizes of 1° and 15 days, respectively, and a requirement of minimum 30 matchups per bin. The 95% confidence intervals are shown as shaded areas (mainly visible at high latitudes).

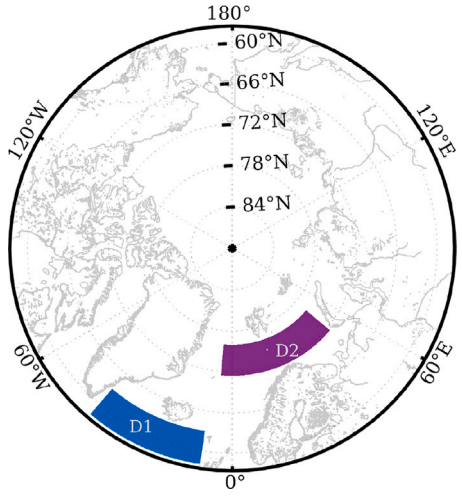

Fig. 10. Domain 1 (D1, blue) and 2 (D2, magenta) used for the calculation of the spectral power.

also enable an identification of any inconsistencies/spurious effects in the PMW SST data ingestion.

The estimation of the power spectrum is performed using the standard FFT method in the zonal direction (Thomson and Emery, 2014) and only open water points are included. The power spectrum per wave number is computed for each latitude band and averaged into bins for the full year for each test run. Fig. 11 shows the zonal spectra for each test run (except from IR_PMW* for which there was no visible difference from IR*_PMW) during 2015 for sub-domains D1 (a) and D2 (b). The theoretical −2 and −5/3 (−1.6) curves for the expected decrease of spectral power in the mesoscale to sub-mesoscale are also included for Vazquez-Cuervo et al. (2022), Castro et al. (2017). Note that the smallest scales are resolved only in the northernmost region of the D2 domain, as the distance between meridionals becomes smaller towards the high latitudes. This means that the results for the smallest scales are based on less data than for the larger scales. Therefore, to avoid noisy signals, only power spectra with wavelengths larger than 6 km are shown. Generally, the effective spatial resolution of the test runs follows the expected theoretical behaviour for the sub-mesoscale and is comparable with that of other L4 products (Vazquez-Cuervo et al., 2022; Castro et al., 2017).

Fig. 11 shows similar power spectra at scales larger than ~60 km for D1 and scales larger than ~20 km for D2, for the different test runs. The "bump" in spectral power occurring for the PMW and IR_PMW at approximately 12.5 km in D1 (10.5 km in D2) is assumed to be associated with energy contribution from the smaller scales, probably due to the mismatch between the native resolution of the L2 PMW data (10 km) and the L3/L4 grid spacing (0.05 degrees). For PMW and IR_PMW, this mismatch leaves gaps in approximately every second L3 grid cell after one satellite overpass, while additional overpasses likely fill in some of the same, but also alternative (every second) L3 grid cells. As a result, any SST bias variations between orbits may introduce spurious energy at smaller scales and this is likely what is seen here. PMW and IR_PMW generally have more energy at small scales compared to the other test runs and their spectral slopes are gentler, i.e. slower decrease in power as wavenumbers increase. This is likely explained by the fact that both of these test runs include PMW SST observations (approximately for every tenth kilometer) in regions that were otherwise under-sampled by IR (and gap-filled using OI). This is in contrast to IR_PMW_SUB and IR*_PMW, where the PMW SSTs have been subsampled and the L4 output relies more on the interpolation capability in these regions resulting in a more smooth L4 field. This is manifested as an overall lower spectral power level and a rapid decrease in the power as wavenumbers increase, i.e. steeper spectral slopes. In IR_PMW_AVG, the averaging performed in the aggregation of the L3 PMW SST field also results in a more smooth L4 SST field. Except from PMW and IR_PMW, the test runs are closely aligned with the IR spectra (i.e. indicating no degradation of the effective spatial resolution when including the PMW SST data), which is ideal in terms of long-term consistency of a merged IR and PMW SST product.

4.4. Selection for the CDR

Different ways of including PMW SST observations in the L4 Arctic SST/IST reanalysis have been assessed. For all test runs, the inclusion of PMW SSTs reduces the L4 standard deviations against drifters compared to only using IR SST (and only using PMW SST).

The best L3 PMW validation result is obtained by allowing each L2 PMW observation to be included in all L3 grid cells in a radius of 5 km from the L2 PMW observation. This reduces the noise and provides more robust L3 PMW SST estimates (see IR_PMW_AVG validation in Section 4.2). To reduce the dependence between the L3 PMW observations and the risk of PMW flooding in the OI scheme, this L3 PMW field (from IR_PMW_AVG) has been sub-sampled by only including those grid cells, which were also included in IR_PMW_SUB. This is done in both IR*_PMW and IR_PMW* that differ only in the inter-sensor bias correction, which adjusts the PMW SST to IR SST in IR*_PMW and IR SST to PMW SST in IR_PMW*. The smallest discrepancy against drifters is seen in the case where the IR SSTs are adjusted to PMW SSTs, since the IR SSTs are generally too cold compared to drifters. However, the PMW observations span a much shorter time scale than IR, which limits the extent to which the bias correction against PMW

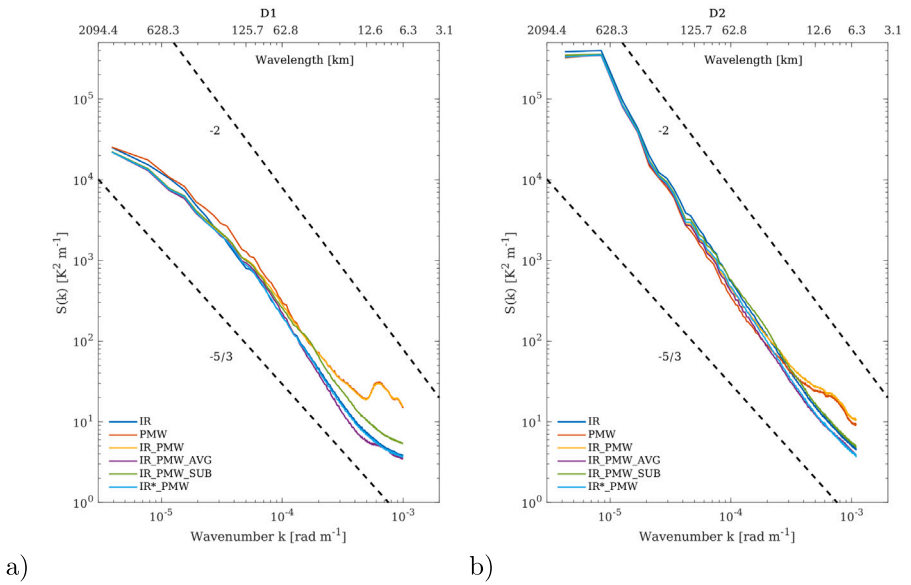

Fig. 11. Zonal power spectra for the subdomains (a) D1 and (b) D2 for the different test runs during 2015.

SSTs can be applied. To increase the feasibility of climate analyses, we have decided to adjust the PMW SSTs to IR SSTs to ensure consistency and avoid jumps when introducing the PMW SSTs in a long-term SST analysis (i.e. 1982-present).

The spectral analysis revealed similar zonal spectra for all the test runs (and both domains) except from PMW and IR_PMW, which both have more energy in the small-scales compared to the other test runs. This is explained by the fact that both of these test runs include PMW SST observation (approximately for every tenth kilometer) in regions that were otherwise under-sampled by IR. The other test runs are closely aligned with the IR spectra, which is ideal in terms of long-term consistency of a merged IR and PMW SST product.

Based on above analyses, we decided to use the setup from IR*_PMW to generate a blended IR and PMW Arctic L4 SST CDR for the ESA CCI PMW SST CDR period extending from June 2002 to October 2017.

5. CDR results

This section provides the validation and uncertainty results of the blended Arctic IR and PMW L4 SST CDR for the ESA CCI PMW SST period (2002–2017), hereafter referred to as IR*_PMW (after the test run, which it is based on). The results of the full IR*_PMW SST CDR is compared to the IR-based Arctic SST/IST CDR (described in Nielsen-Englyst et al., 2023) for this period, which will be referred to as IR hereafter. In the PMW sensor gap between AMSR-E and AMSR2 (from October 4, 2011 to July 4, 2012) the IR*_PMW SST CDR is based only on IR observations, and is thus identical to the IR SST CDR for this period.

5.1. Validation

The long-term IR and IR*_PMW runs have been validated against drifting buoys, Argo floats and moorings for the years 2002–2017. The validation statistics are summarized in Table 3 for the L3S and L4 SST products. For both drifters and Argo floats there is a substantial improvement in the L4 standard deviations, which reduce from 0.54 °C to 0.47 °C and from 0.47 °C to 0.41 °C, respectively, by including PMW SST observations. Moorings show very limited variation in the L4 performances and this is explained by the fact that the moorings are located only in specific parts of the North Atlantic and the southern Greenland Sea.

The L3S SST validation revealed limited variations in the statistics for IR and IR*_PMW (for all *in situ* types). Argo floats and drifters increase their number of L3S matchups with about 15% when PMW observations are added, while moorings only have 4% more matchups when including PMW observations. These additional matchups are not available for the IR product, and if these matchups are excluded from the L3S IR*_PMW validation, the statistical parameters (provided in Table 3) of L3S IR and L3S IR*_PMW are the exact same (for all *in situ* types).

Fig. 12(a) shows the geographical distribution of standard deviation against drifters for L4 IR*_PMW, while Fig. 12(b) shows the differences in standard deviation between L4 IR*_PMW and L4 IR for drifters during the period 2002–2017. The largest standard deviations are generally found along the coasts and sea ice edge, where few IR and PMW SSTs are available. Compared to the IR run, the inclusion of PMW SSTs provides reduced standard deviations in almost all regions with few exceptions which are likely related to sea ice contamination and residual RFI (Gentemann and Hilburn, 2015).

Fig. 13(a) shows the annual mean and standard deviation of the L4 SST minus drifter SST differences for the period 2002–2017. In general, higher standard deviations are seen when no PMW SST observations are included. For both IR and IR*_PMW, the standard deviations are largest in the last part of the period (2011–2017), which is characterized by fewer IR SST observations, since the (A)ATSR and SLSTR are not available (Nielsen-Englyst et al., 2023; Merchant et al., 2019). For this period, we also notice a larger reduction in standard deviation when including PMW SSTs. At the same time, the mean difference differs slightly among the two runs, which was unexpected as the PMW SSTs have been adjusted to the IR SSTs. To investigate this effect in greater detail, Fig. 13(b) shows the validation statistics as a function of the number of days since an IR SST observation was last available in that particular grid cell. For both IR and IR*_PMW, the standard deviations against drifters increase almost linearly with the number of days since an IR SST observation was last available. It is also seen that the reduction in standard deviation from including PMW SSTs increases with the number of days since the last IR observation (i.e. the largest improvements are seen in IR data sparse regions). The mean difference aligns well for the two test runs in cases where IR observations have been available within the last 50 days. For those matchups (2%) where IR observations are lacking in more than 60 days, the mean difference (against drifters) differs among the two runs, with the mean difference for the IR product tending to 0 °C. This

Table 3
Overall performance of IR and IR*_PMW SSTs against drifting buoys, Argo floats and moorings for the years 2002–2017. The table shows the mean difference (MD; provided as the satellite fields minus *in situ*), standard deviation of the differences (STD), root mean squared difference (RMSE), and the number of observations (Nobs). A 3-sigma filter has been applied to remove outliers.

	L4 IR				L4 IR*_PMW				L3S IR				L3S IR*_PMW			
	MD	STD	RMSE	Nobs	MD	STD	RMSE	Nobs	MD	STD	RMSE	Nobs	MD	STD	RMSE	Nobs
Drifters	−0.15	0.54	0.56	1.70e06	−0.15	0.47	0.49	1.70e06	−0.09	0.42	0.43	4.62e05	−0.11	0.42	0.43	5.31e05
Moorings	−0.11	0.55	0.56	39,935	−0.12	0.54	0.56	39,935	−0.05	0.51	0.51	16,649	−0.06	0.52	0.52	17,304
Argo	−0.07	0.47	0.48	19,847	−0.06	0.41	0.41	19,936	0.01	0.38	0.38	5,758	−0.00	0.38	0.38	6,578

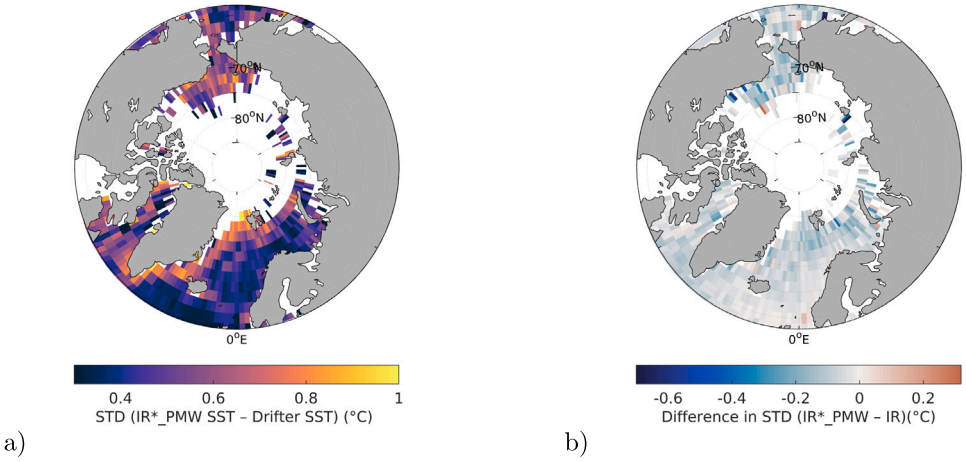

Fig. 12. (a) Standard deviation (STD) of the L4 SST differences against drifter SST for IR*_PMW and (b) the difference in standard deviation between L4 IR*_PMW and IR for drifters, during the period 2002–2017. The statistics are calculated for each 2 × 2 degree grid having more than 50 members.

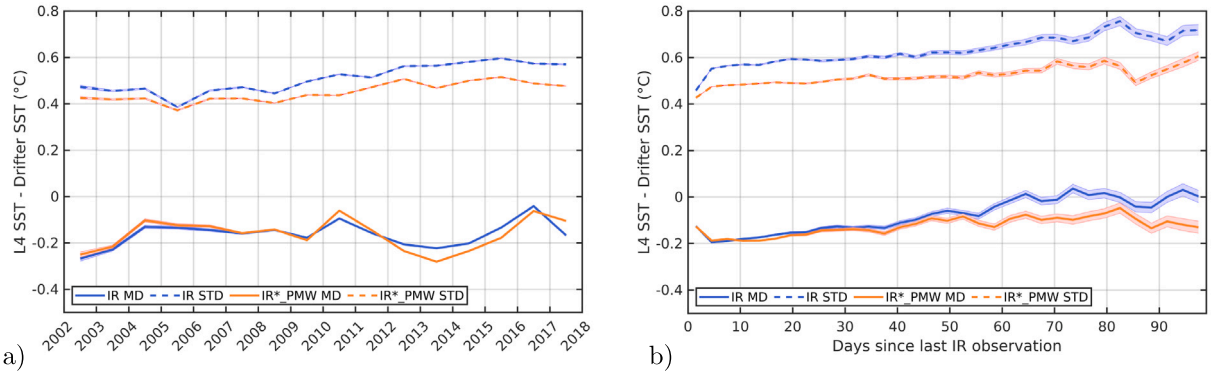

Fig. 13. Mean differences (MD) and standard deviations (STD) of the differences against drifter SST for IR and IR*_PMW CDR SSTs as a function of (a) time and (b) days since last IR observation, using bin sizes of one year and three days, respectively, and a requirement of minimum 30 matchups per bin. The 95% confidence intervals are shown as shaded areas (mainly visible for the large number of days since last IR observation.

is a phenomenon occurring mainly from October through December, when long periods without observations result in the use of first guess (previous day's analysis) many days in a row, resulting in the use of erroneously warmer (summer+fall) SSTs. In principle, the OI should account for this by taking neighbour observations into account but what we see is the residual effect from large areas with missing observations for a long time. This is of course undesirable and will be discussed further in Section 6. The inclusion of the more frequent PMW SSTs reduces this effect as seen in Fig. 13(b). This is another advantage of including PMW observations with frequent updates from past, current and future PMW radiometers.

5.2. L4 uncertainty

As described in Nielsen-Englyst et al. (2023) each daily L4 SST/IST is assigned with an uncertainty estimate, which is a direct output of the OI method that depends on the data availability, the proximity of the observations and the uncertainty of the observations and the background field. Fig. 14(a) shows the geographical mean L4 SST uncertainty for IR*_PMW for the period 2002–2017. The largest uncertainties are found along the coasts and in the seasonal ice covered regions with maximum uncertainties (of ~2 °C) north of Svalbard. This is in agreement with the increased standard deviations observed against drifters in this region (Fig. 12(a)). Fig. 14(b) shows the reduction in L4 SST uncertainty when including PMW SST observations, with the largest reductions in the Barents Sea, Greenland Sea and the Labrador Sea.

Fig. 15 shows the yearly mean L4 SST uncertainty during 2002–2017 for IR and IR*_PMW, respectively. In both cases, the L4 SST uncertainty increases after 2011 as a result of fewer IR satellite observations which is in agreement with the increased standard deviations observed in the end of the record in Fig. 13(a). At all times, the IR*_PMW provides lower L4 SST uncertainties than the IR run, with the largest improvements in the end of the period, which is also in

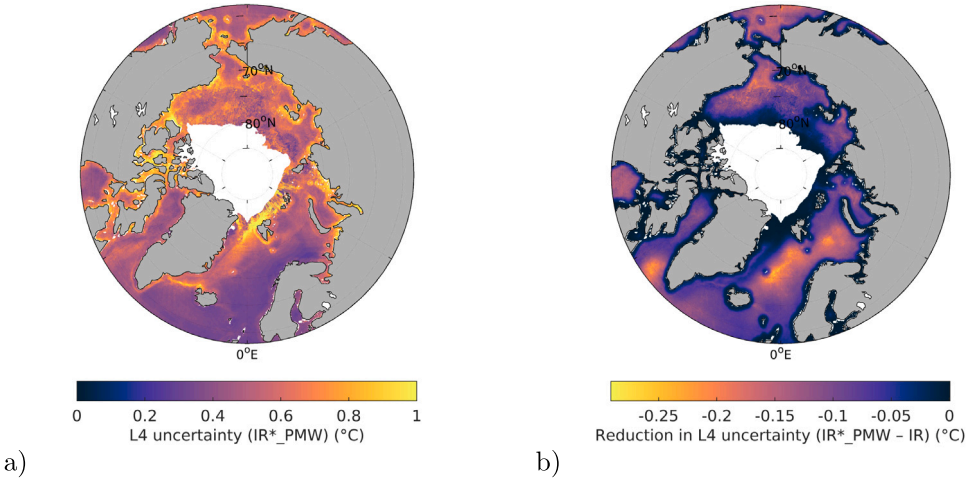

Fig. 14. Spatial mean (a) L4 SST uncertainty of IR*_PMW and (b) L4 SST uncertainty difference between IR*_PMW and IR calculated for grid cells with more than 90 days of open water in the period 2002–2017.

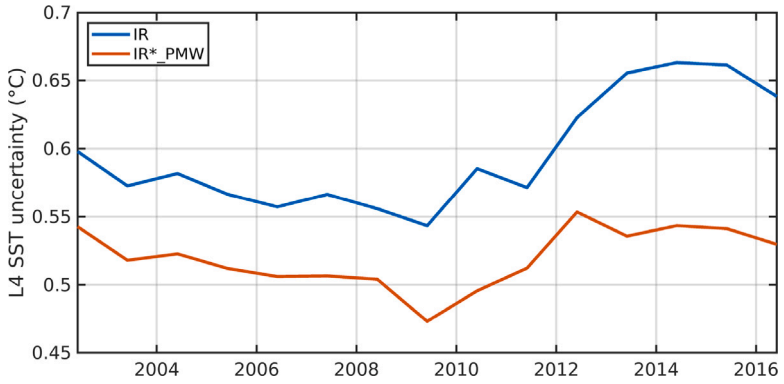

Fig. 15. Yearly mean L4 SST uncertainty during 2002–2017 for IR and IR*_PMW.

agreement with Fig. 13(a). Overall, IR*_PMW provides a reduction in the L4 SST uncertainty of 0.08 °C compared to IR, which is comparable to the reduction in standard deviation observed against drifters of 0.07 °C (see Table 3). Nielsen-Englyst et al. (2023) also showed good agreement between L4 SST uncertainties and observed uncertainties using drifter SSTs as reference for the full IR record (1982–2021). The reduced L4 SST uncertainty estimates obtained when including PMW SSTs are thus very promising results.

6. Discussion

The inclusion of PMW SST observations provides substantial reductions in the L4 standard deviations compared to only using IR (and only using PMW) SST observations. The improved performance is mainly linked to the superior coverage from PMW observations in the Arctic (Fig. 7). However, the independent and highly complementary uncertainty characteristics of PMW and IR observations (see Section 3) are likely also part of the explanation for the observed improvements. The complementary uncertainty characteristics reduce the risk of systematic biases (e.g. as seen for the IR) in a merged product. This is supported by all combinations of IR and PMW SSTs (without introducing an inter-sensor bias correction) having reduced L4 biases compared to the IR test run (Table 2). The colder temperatures observed in the Arctic IR SSTs (compared to drifters) is a well known problem, which is also seen in other SST analyses e.g. OSTIA (Fiedler et al., 2019). To reduce the risk of introducing biases when switching from one sensor to the other/or both, an inter-sensor bias correction is necessary. Fig. 6 shows an example of the mean inter-sensor bias correction applied during 2015, with a distinct seasonal cycle. An analysis of the bias correction during the full record (2002–2017) revealed similar seasonal patterns, but also large inter-annual variations. This challenges the derivation of a generic bias correction to be used outside of the PMW SST period. When applying the dynamic bias correction (Section 3.8), the smallest L4 mean difference against drifters is seen in the case where the IR SSTs are adjusted to PMW SSTs. However, to be consistent with time periods when no Arctic PMW SSTs are available, the bias correction adjusting the PMW SSTs to IR SST has been implemented here. This introduces a bias in the L4 SST as seen in Table 2. Since, the continuity of PMW imagers have been sustained for the future with AMSR3 and CIMR in the pipeline, future work should focus on using the PMW SST observations to adjust the cold IR SSTs in the Arctic (also extended to periods when no PMW SSTs are available).

In general, the largest standard deviations (Fig. 12(a)) and theoretical uncertainties (Fig. 14(a)) are found along the coasts and sea ice edge for both IR and IR*_PMW as well as for the other test runs (not shown). In these regions, few or no SST observations from the IR and PMW satellite sensors (Fig. 3) make it challenging to provide accurate SST estimates. In addition, some of these regions have very large gradients in the surface temperature e.g. along the ice edge (Carvalho and Wang, 2020). The improved spatial resolution (of 15 km) from CIMR will enable PMW SST retrievals much closer to coasts and sea ice in the future. The higher accuracy of 0.3 °C (in cold waters) from CIMR will also improve the Arctic SST estimates even further.

The L4 IR standard deviations during 2015 were higher (0.64 °C for drifters) compared to those from the full period (0.54 °C for drifters). This is mainly explained by the fact that only the AVHRR sensors

were available during the period 2011–2017 (Nielsen-Englyst et al., 2023; Merchant et al., 2019). The year, 2015, was chosen since we expected the largest impact from PMW observations to occur when few IR observations are available, thus making it more feasible to assess the impact and variations among the different test runs. As evident from Fig. 13(a), the largest reduction in standard deviation by including PMW SSTs was indeed observed during the period 2011–2017. In relation to that, Fig. 13(b) also showed that the reduction in standard deviation is largest for regions rarely observed by IR sensors.

For both IR and IR*_PMW, the reduced satellite coverage during 2011–2017 resulted in increased standard deviations (Fig. 13(a)) and increased L4 uncertainties (Fig. 15). In the same period, the mean difference differs between IR and IR*_PMW and the explanation for this is the difference in the satellite coverage. The overall mean differences reported in Nielsen-Englyst et al. (2023) did not show any long-term dependence on the satellite coverage (i.e. considering the generally increasing satellite coverage over time). However, Fig. 13(b) revealed that there is a coverage dependence when binning the mean differences as a function of the days since the last IR observation in that particular grid point. Both IR and IR*_PMW get warmer as the number of consecutive days without IR observations increases. The issue arises during fall and early winter in unobserved regions and when the surrounding observations are too far away to have any weight in the OI scheme. In that case, the first guess SST (i.e. previous day's analysis in this case) is used many days in succession resulting in the use of erroneous warmer (summer and fall) SSTs.

This is clearly undesirable, in particular in the context of climate monitoring. Most of the existing and widely used L4 global SST analyses also use OI techniques (Castro et al., 2016; Vazquez-Cuervo et al., 2022) and the previous day's analysis as first guess (e.g. NOAA OI SST and REMSS MW-IR SST), and it is thus likely that they also are affected by this artefact. Fig. 13(b) showed that the residual effect was most pronounced when only including IR observations, while the inclusion of the PMW observations reduced the effect. This is another argument of including the more frequent available PMW observations from past, present and future missions. However, despite the inclusion of PMW SSTs, the problem will likely persist in regions very near coasts and sea ice, which cannot be resolved by the current IR and PMW sensors. This should be addressed in future updates of the Arctic reanalysis as well as in the development of new regional and global reanalyses e.g. by applying a seasonal variation to the first guess field.

Another suggestion for future work is a detailed assessment of the changes in the spatial SST gradients in terms of intensity and location, when including PMW SST observations. In this study, an initial investigation has been conducted by running a Sobel operator on the SST fields from test run IR and IR*_PMW and considering the difference in the gradient magnitude fields for the full year (i.e. 2015). Some changes in the intensity and location of the SST gradients are seen e.g. a reduction in the SST gradients in proximity to sea ice when including PMW SST observations (not shown), but the mean difference is very small. Further analysis is needed to fully understand why these differences arise and taking into account the varying grid sizes in the region.

Future work should also be focused towards improving the validation close to sea ice e.g. by using Saildrone observations (Gentemann et al., 2020; Vazquez-Cuervo et al., 2022; Jia et al., 2022) and potentially improving the surface temperature estimates close to both coasts and the sea ice e.g. in similar ways as done for salinity retrievals in Meissner and Manaster (2021) and Olmedo et al. (2017). Moreover, the capability of using PMW ISTs to supplement the IR ISTs should also be investigated in the future. An increasing number of PMW derived IST products have become available at daily temporal resolution based on the vertically polarized 6.9-GHz channel AMSR-data (e.g. Le Traon et al., 2015; Comiso et al., 2003; Kilic et al., 2019). These approximately represent the physical temperature of the snow/ice interface (Tonboe et al., 2011; Tonboe, 2010; Ulaby et al., 1986), and relating these to IR IST (i.e. the skin surface temperature) is a challenging task considering the large temperature gradients in the snow during winter (e.g. Comiso et al., 2003, 1989).

Finally, future work should aim at updating the OI scheme to include the L2 PMW SST uncertainty estimates provided with the individual PMW SST retrievals instead of the spatial and temporal constant of 0.5 °C. Alerskans et al. (2020) showed good validation results of the L2 PMW SST uncertainties and using these may lead to better L4 SST estimates as well as improved L4 uncertainty estimates.

7. Conclusions

The impact of including passive microwave (PMW) sea surface temperature (SST) observations is investigated using an existing infrared (IR) gap-free (L4) Arctic surface temperature analysis covering the ocean and sea ice northwards of 58°N. The Arctic suffers from frequent and persistent cloud cover, which prevents IR retrievals of SST. Therefore, the almost all-weather PMW sensors have a significant coverage advantage over IR sensors (which nevertheless provide a much better spatial resolution).

This study provides a systematic assessment of how to best combine IR and PMW SST observations in a blended L4 Arctic SST analysis in order to improve existing reanalyses as well as preparing for future PMW missions (such as CIMR). It is found that the addition of PMW SST observations improves the L4 SST validation results against drifting buoy SSTs for all the methods evaluated here. In order to combine IR and PMW, it is important to correct for systematic biases in the PMW and IR SST data sets relative to each other. The PMW SSTs show lower mean differences against drifter SSTs compared to the IR SSTs, but for consistency with time periods when no Arctic PMW SST observations are available, the PMW SSTs have been adjusted to IR SSTs in this study. This has been done in order to generate a blended IR and PMW Arctic SST climate dataset for the ESA-CCI PMW SST data period (2002–2017).

The overall L4 SST standard deviations decrease from 0.54 °C, 0.55 °C and 0.47 °C to 0.47 °C, 0.54 °C and 0.41 °C against drifters, moorings and Argo floats, respectively, when PMW SST observations are included in the full record (2002–2017). As expected, the largest improvements are seen when the IR data is sparse, but improved performance is seen in almost all regions including those already covered by IR observations. The good performance is likely not only due to the superior PMW coverage but also related to the different and complementary uncertainty characteristics of IR and PMW observations. The mean theoretical uncertainty estimate decreases with 0.08 °C when including PMW observations, which is in good agreement with the observed reduction in standard deviation against drifters.

The largest theoretical uncertainties and standard deviations against drifters are generally found along the sea ice edge and coasts, which suffer from no or few SST observations (both from IR and PMW sensors). Improved PMW coverage and SST retrievals are expected in the future with the launch of the CIMR mission, which will provide SSTs with a spatial resolution of 15 km and a precision of 0.3 °C (in cold waters) (Donlon, 2020). This will allow PMW SST retrievals much closer to the coasts and sea ice compared to what is possible with previous and current radiometers. Therefore, CIMR has a very large potential to improve Arctic SST estimates even further.

CRediT authorship contribution statement

Pia Nielsen-Englyst: Conceptualization, Data curation, Formal analysis, Investigation, Methodology, Software, Validation, Visualization, Writing – original draft, Writing – review & editing. **Jacob L. Høyer:** Conceptualization, Funding acquisition, Methodology, Resources, Supervision, Writing – review & editing. **Ioanna Karagali:** Data curation, Formal analysis, Investigation, Software, Visualization, Writing – original draft, Writing – review & editing. **Wiebke M. Kolbe:** Data curation, Software, Writing – review & editing. **Rasmus T. Tonboe:** Supervision, Writing – review & editing. **Leif T. Pedersen:** Supervision, Writing – review & editing.

Declaration of competing interest

The authors declare that they have no known competing financial interests or personal relationships that could have appeared to influence the work reported in this paper.

Data availability

Data will be made available on request.

Acknowledgements

This work is funded by the Copernicus Marine Environment Monitoring Service (CMEMS) and the Danish National Centre for Climate Research (NCKF) at the Danish Meteorological Institute (DMI). The PMW SST CDR has been developed within the European Space Agency's Climate Change Initiative for Sea Surface Temperature project under grant number 4000109848/13/I-NB.

References

Alerskans, E., Høyer, J.L., Gentemann, C.L., Pedersen, L.T., Nielsen-Englyst, P., Donlon, C., 2020. Construction of a climate data record of sea surface temperature from passive microwave measurements. Remote Sens. Environ. 236, 111485.

Alerskans, E., Zinck, A.-S.P., Nielsen-Englyst, P., Høyer, J.L., 2022. Exploring machine learning techniques to retrieve sea surface temperatures from passive microwave measurements. Remote Sens. Environ. 281, 113220.

AMAP, 2021. Arctic climate change update 2021: Key trends and impacts. Summary for policy-makers.

Atkinson, C.P., Rayner, N.A., Kennedy, J.J., Good, S.A., 2014. An integrated database of ocean temperature and salinity observations. J. Geophys. Res.: Oceans 119 (10), 7139–7163.

Bojinski, S., Verstraete, M., Peterson, T.C., Richter, C., Simmons, A., Zemp, M., 2014. The concept of essential climate variables in support of climate research, applications, and policy. Bull. Am. Meteorol. Soc. 95 (9).

Brasnett, B., 2008. The impact of satellite retrievals in a global sea-surface-temperature analysis. Q. J. R. Meteorol. Soc. 134 (636), 1745–1760.

Brasnett, B., Colan, D.S., 2016. Assimilating retrievals of sea surface temperature from VIIRS and AMSR2. J. Atmos. Ocean. Technol. 33 (2), 361–375.

Carvalho, K., Wang, S., 2020. Sea surface temperature variability in the Arctic Ocean and its marginal seas in a changing climate: Patterns and mechanisms. Glob. Planet. Change 193, 103265.

Castro, S.L., Emery, W.J., Wick, G.A., Tandy Jr., W., 2017. Submesoscale sea surface temperature variability from UAV and satellite measurements. Remote Sens. 9 (11), 1089.

Castro, S.L., Wick, G.A., Jackson, D.L., Emery, W.J., 2008. Error characterization of infrared and microwave satellite sea surface temperature products for merging and analysis. J. Geophys. Res.: Oceans 113 (C3).

Castro, S.L., Wick, G.A., Steele, M., 2016. Validation of satellite sea surface temperature analyses in the Beaufort Sea using UpTempO buoys. Remote Sens. Environ. 187, 458–475.

Centurioni, L.R., Turton, J., Lumpkin, R., Braasch, L., Brassington, G., Chao, Y., Charpentier, E., Chen, Z., Corlett, G., Dohan, K., et al., 2019. Global in situ observations of essential climate and ocean variables at the air–sea interface. Front. Mar. Sci. 419.

Chin, T.M., Vazquez-Cuervo, J., Armstrong, E.M., 2017. A multi-scale high-resolution analysis of global sea surface temperature. Remote Sens. Environ. 200, 154–169.

Comiso, J.C., Cavalieri, D.J., Markus, T., 2003. Sea ice concentration, ice temperature, and snow depth using AMSR-E data. IEEE Trans. Geosci. Remote Sens. 41 (2), 243–252.

Comiso, J., Grenfell, T., Bell, D., Lange, M., Ackley, S., 1989. Passive microwave in situ observations of winter Weddell Sea ice. J. Geophys. Res.: Oceans 94 (C8), 10891–10905.

Dash, P., Ignatov, A., Martin, M., Donlon, C., Brasnett, B., Reynolds, R.W., Banzon, V., Beggs, H., Cayula, J.-F., Chao, Y., et al., 2012. Group for high resolution sea surface temperature (GHRSST) analysis fields inter-comparisons—Part 2: Near real time web-based level 4 SST quality monitor (L4-SQUAM). Deep Sea Res. Part II 77, 31–43.

Donlon, C., 2020. Copernicus imaging microwave radiometer (CIMR) mission requirements document, version 4. ref. ESA-EOPSM-CIMR-MRD-3236, European Space Agency, Noordwijk, The Netherlands.

Donlon, C., Casey, K., Gentemann, C., LeBorgne, P., Robinson, I., Reynolds, R., Merchant, C., Llewellyn-Jones, D., Minnett, P., Piolle, J., et al., 2009. Successes and challenges for the modern sea surface temperature observing system. Community White Paper for OceanObs, 9, pp. 1–9.

Donlon, C.J., Martin, M., Stark, J., Roberts-Jones, J., Fiedler, E., Wimmer, W., 2012. The operational sea surface temperature and sea ice analysis (OSTIA) system. Remote Sens. Environ. 116, 140–158.

Donlon, C., Robinson, I., Casey, K., Vazquez-Cuervo, J., Armstrong, E., Arino, O., Gentemann, C., May, D., LeBorgne, P., Piollé, J., et al., 2007. The global ocean data assimilation experiment high-resolution sea surface temperature pilot project. Bull. Am. Meteorol. Soc. 88 (8), 1197–1214.

Dybkjær, G., Eastwood, S., Borg, A., Høyer, J., Tonboe, R., 2018. Algorithm theoretical basis document (ATBD) for the OSI SAF Sea and Sea Ice Surface Temperature L2 processing chain, OSI205a and b.

Dybkjær, G., Høyer, J., Tonboe, R., Olsen, S., 2014. Report on the documentation and description of the new Arctic Ocean dataset combining SST and IST, NACLIM Deliverable D32. 28.

Embury, O., Merchant, C.J., Corlett, G.K., 2012. A reprocessing for climate of sea surface temperature from the along-track scanning radiometers: Initial validation, accounting for skin and diurnal variability effects. Remote Sens. Environ. 116, 62–78.

Fiedler, E., Mao, C., Good, S., Waters, J., Martin, M., 2019. Improvements to feature resolution in the OSTIA sea surface temperature analysis using the NEMOVAR assimilation scheme. Q. J. R. Meteorol. Soc. 145 (725), 3609–3625.

Gentemann, C.L., 2014. Three way validation of MODIS and AMSR-E sea surface temperatures. J. Geophys. Res.: Oceans 119 (4), 2583–2598.

Gentemann, C.L., Hilburn, K.A., 2015. In situ validation of sea surface temperatures from the GCOM-W 1 AMSR 2 RSS calibrated brightness temperatures. J. Geophys. Res.: Oceans 120 (5), 3567–3585.

Gentemann, C., Scott, J.P., Mazzini, P.L., Pianca, C., Akella, S., Minnett, P.J., Cornillon, P., Fox-Kemper, B., Cetinić, I., Chin, T.M., et al., 2020. Saildrone: Adaptively sampling the marine environment. Bull. Am. Meteorol. Soc. 101 (6), E744–E762.

Good, S., Fiedler, E., Mao, C., Martin, M.J., Maycock, A., Reid, R., Roberts-Jones, J., Searle, T., Waters, J., While, J., et al., 2020. The current configuration of the OSTIA system for operational production of foundation sea surface temperature and ice concentration analyses. Remote Sens. 12 (4), 720.

Horrocks, L.A., Candy, B., Nightingale, T.J., Saunders, R.W., O'Carroll, A., Harris, A.R., 2003. Parameterizations of the ocean skin effect and implications for satellite-based measurement of sea-surface temperature. J. Geophys. Res.: Oceans 108 (C3).

Høyer, J.L., Karagali, I., Dybkjær, G., Tonboe, R., 2012. Multi sensor validation and error characteristics of Arctic satellite sea surface temperature observations. Remote Sens. Environ. 121, 335–346.

Høyer, J.L., Le Borgne, P., Eastwood, S., 2014. A bias correction method for Arctic satellite sea surface temperature observations. Remote Sens. Environ. 146, 201–213.

Huang, B., Liu, C., Banzon, V., Freeman, E., Graham, G., Hankins, B., Smith, T., Zhang, H.-M., 2021. Improvements of the daily optimum interpolation sea surface temperature (DOISST) version 2.1. J. Clim. 34 (8), 2923–2939.

Jia, C., Minnett, P.J., 2020. High latitude sea surface temperatures derived from MODIS infrared measurements. Remote Sens. Environ. 251, 112094.

Jia, C., Minnett, P.J., Szczodrak, M., Izaguirre, M., 2022. High latitude sea surface skin temperatures derived from saildrone infrared measurements. IEEE Trans. Geosci. Remote Sens..

Kasahara, M., Kachi, M., Inaoka, K., Fujii, H., Kubota, T., Shimada, R., Kojima, Y., 2020. Overview and current status of GOSAT-GW mission and AMSR3 instrument. In: Sensors, Systems, and Next-Generation Satellites XXIV. Vol. 11530, SPIE, 1153007.

Kilic, L., Tonboe, R.T., Prigent, C., Heygster, G., 2019. Estimating the snow depth, the snow–ice interface temperature, and the effective temperature of Arctic sea ice using Advanced Microwave Scanning Radiometer 2 and ice mass balance buoy data. Cryosphere 13 (4), 1283–1296.

Lavergne, T., Kern, S., Aaboe, S., Derby, L., Dybkjaer, G., Garric, G., Heil, P., Hendricks, S., Holfort, J., Howell, S., et al., 2022. A new structure for the sea ice essential climate variables of the Global Climate Observing System. Bull. Am. Meteorol. Soc. 103 (6), E1502–E1521.

Le Traon, P.-Y., Antoine, D., Bentamy, A., Bonekamp, H., Breivik, L., Chapron, B., Corlett, G., Dibarboure, G., DiGiacomo, P., Donlon, C., et al., 2015. Use of satellite observations for operational oceanography: recent achievements and future prospects. J. Oper. Oceanogr. 8 (sup1), s12–s27.

Liu, Y., Minnett, P.J., 2016. Sampling errors in satellite-derived infrared sea-surface temperatures. Part I: Global and regional MODIS fields. Remote Sens. Environ. 177, 48–64.

Meissner, T., Manaster, A., 2021. SMAP salinity retrievals near the sea-ice edge using multi-channel AMSR2 brightness temperatures. Remote Sens. 13 (24), 5120.

Merchant, C.J., Embury, O., Bulgin, C.E., Block, T., Corlett, G.K., Fiedler, E., Good, S.A., Mittaz, J., Rayner, N.A., Berry, D., et al., 2019. Satellite-based time-series of sea-surface temperature since 1981 for climate applications. Sci. Data 6 (1), 1–18.

Merchant, C.J., Embury, O., Roberts-Jones, J., Fiedler, E., Bulgin, C.E., Corlett, G.K., Good, S., McLaren, A., Rayner, N., Morak-Bozzo, S., et al., 2014. Sea surface temperature datasets for climate applications from Phase 1 of the European Space Agency Climate Change Initiative (SST CCI). Geosci. Data J. 1 (2), 179–191.

Meredith, M., Sommerkorn, M., Cassotta, S., Derksen, C., Ekaykin, A., Hollowed, A., Kofinas, G., Mackintosh, A., Melbourne-Thomas, J., Muelbert, M., Ottersen, G., Schuur, E., 2019. Polar regions. In: Pörtner, H.-O., Roberts, D., Masson-Delmotte, V., Zhai, P., Tignor, M., Poloczanska, E., Mintenbeck, K., Alegría, A., Nicolai, M., Okem, A., Petzold, J., Rama, B., Weyer, N. (Eds.), IPCC Special Report on the Ocean and Cryosphere in a Changing Climate. In press.

Minnett, P., Alvera-Azcárate, A., Chin, T., Corlett, G., Gentemann, C., Karagali, I., Li, X., Marsouin, A., Marullo, S., Maturi, E., et al., 2019. Half a century of satellite remote sensing of sea-surface temperature. Remote Sens. Environ. 233, 111366.

Minnett, P., Kaiser-Weiss, A., 2012. Group for high resolution sea-surface temperature discussion document: Near-surface oceanic temperature gradients.

Nielsen-Englyst, P., Høyer, J.L., Kolbe, W.M., Dybkjær, G., Lavergne, T., Tonboe, R.T., Skarpalezos, S., Karagali, I., 2023. A combined sea and sea-ice surface temperature climate dataset of the Arctic, 1982–2021. Remote Sens. Environ. 284, 113331.

Nielsen-Englyst, P., L Høyer, J., Toudal Pedersen, L., L Gentemann, C., Alerskans, E., Block, T., Donlon, C., 2018. Optimal estimation of sea surface temperature from AMSR-E. Remote Sens. 10 (2), 229.

O'Carroll, A.G., Armstrong, E.M., Beggs, H.M., Bouali, M., Casey, K.S., Corlett, G.K., Dash, P., Donlon, C.J., Gentemann, C.L., Høyer, J.L., et al., 2019. Observational needs of sea surface temperature. Front. Mar. Sci. 6, 420.

O'Carroll, A.G., Eyre, J.R., Saunders, R.W., 2008. Three-way error analysis between AATSR, AMSR-E, and in situ sea surface temperature observations. J. Atmos. Ocean. Technol. 25 (7), 1197–1207.

Olmedo, E., Martínez, J., Turiel, A., Ballabrera-Poy, J., Portabella, M., 2017. Debiased non-Bayesian retrieval: A novel approach to SMOS Sea Surface Salinity. Remote Sens. Environ. 193, 103–126.

Pithan, F., Mauritsen, T., 2014. Arctic amplification dominated by temperature feedbacks in contemporary climate models. Nat. Geosci. 7 (3), 181–184.

Rantanen, M., Karpechko, A.Y., Lipponen, A., Nordling, K., Hyvärinen, O., Ruosteenoja, K., Vihma, T., Laaksonen, A., 2022. The Arctic has warmed nearly four times faster than the globe since 1979. Commun. Earth Environ. 3 (1), 1–10.

Reynolds, R.W., Gentemann, C.L., Corlett, G.K., 2010. Evaluation of AATSR and TMI satellite SST data. J. Clim. 23 (1), 152–165.

Reynolds, R.W., Gentemann, C.L., Wentz, F., 2004. Impact of TRMM SSTs on a climate-scale SST analysis. J. Clim. 17 (15), 2938–2952.

Reynolds, R.W., Rayner, N.A., Smith, T.M., Stokes, D.C., Wang, W., 2002. An improved in situ and satellite SST analysis for climate. J. Climate 15 (13), 1609–1625.

Reynolds, R.W., Smith, T.M., 1994. Improved global sea surface temperature analyses using optimum interpolation. J. Climate 7 (6), 929–948.

Reynolds, R.W., Smith, T.M., Liu, C., Chelton, D.B., Casey, K.S., Schlax, M.G., 2007. Daily high-resolution-blended analyses for sea surface temperature. J. Climate 20 (22), 5473–5496.

Ricciardulli, L., Wentz, F.J., 2004. Uncertainties in sea surface temperature retrievals from space: Comparison of microwave and infrared observations from TRMM. J. Geophys. Res.: Oceans 109 (C12).

Shibata, A., 2006. Features of ocean microwave emission changed by wind at 6 GHz. J. Oceanogr. 62, 321–330.

Thiébaux, J., Rogers, E., Wang, W., Katz, B., 2003. A new high-resolution blended real-time global sea surface temperature analysis. Bull. Am. Meteorol. Soc. 84 (5), 645–656.

Thomson, R.E., Emery, W.J., 2014. Data Analysis Methods in Physical Oceanography. Newnes.

Tonboe, R.T., 2010. The simulated sea ice thermal microwave emission at window and sounding frequencies. Tellus A: Dyn. Meteorol. Oceanogr. 62 (3), 333–344.

Tonboe, R.T., Dybkjær, G., Høyer, J.L., 2011. Simulations of the snow covered sea ice surface temperature and microwave effective temperature. Tellus A: Dyn. Meteorol. Oceanogr..

Ulaby, F., Long, D., Blackwell, W., Elachi, C., Fung, A., Ruf, C., Sarabandi, K., Zebker, H., Van Zyl, J., 2014. Microwave radar and radiometric remote sensing, university of michigan press. Ann Arbor.

Ulaby, F.T., Moore, R.K., Fung, A.K., 1986. Microwave Remote Sensing: Active and Passive. Volume 3- from Theory To Applications.

Vazquez-Cuervo, J., Castro, S.L., Steele, M., Gentemann, C., Gomez-Valdes, J., Tang, W., 2022. Comparison of GHRSST SST analysis in the arctic ocean and Alaskan Coastal waters using saildrones. Remote Sens. 14 (3), 692.

Vincent, R.F., Marsden, R., Minnett, P., Buckley, J., 2008a. Arctic waters and marginal ice zones: 2. An investigation of arctic atmospheric infrared absorption for advanced very high resolution radiometer sea surface temperature estimates. J. Geophys. Res.: Oceans 113 (C8).

Vincent, R.F., Marsden, R., Minnett, P., Creber, K., Buckley, J., 2008b. Arctic waters and marginal ice zones: A composite Arctic sea surface temperature algorithm using satellite thermal data. J. Geophys. Res.: Oceans 113 (C4).

Wentz, F.J., Gentemann, C., Smith, D., Chelton, D., 2000. Satellite measurements of sea surface temperature through clouds. Science 288 (5467), 847–850.

Wentz, F.J., Meissner, T., 2000. Algorithm theoretical basis document(ATBD): AMSR ocean algorithm (version 2). RSS Tech. Proposal 121599A-1, Remote Sensing Systems, Santa Rosa, CA.